

Noise thresholds for optical cluster-state quantum computation

Christopher M. Dawson,¹ Henry L. Haselgrove,^{1,2,*} and Michael A. Nielsen^{1,†}

¹*School of Physical Sciences, The University of Queensland, Queensland 4072, Australia*

²*Information Sciences Laboratory, Defence Science and Technology Organisation, Edinburgh 5111 Australia*

(Dated: September 7, 2018)

In this paper we do a detailed numerical investigation of the fault-tolerant threshold for optical cluster-state quantum computation. Our noise model allows both photon loss and depolarizing noise, as a general proxy for all types of local noise other than photon loss noise. We obtain a *threshold region* of allowed pairs of values for the two types of noise. Roughly speaking, our results show that scalable optical quantum computing is possible for photon loss probabilities $< 3 \times 10^{-3}$, and for depolarization probabilities $< 10^{-4}$. Our fault-tolerant protocol involves a number of innovations, including a method for syndrome extraction known as telecorrection, whereby repeated syndrome measurements are guaranteed to agree. This paper is an extended version of [Dawson et al., Phys. Rev. Lett. **96**, 020501].

PACS numbers: 03.67.-a, 03.67.Lx

I. INTRODUCTION

Optical systems have many significant advantages for quantum computation, such as the ease of performing single-qubit manipulations, long decoherence times, and efficient read-out. Unfortunately, standard linear optical elements alone are unsuitable for quantum computation, as they do not enable photons to interact. This difficulty can, in principle, be resolved by making use of nonlinear optical elements [1, 2], at the price of requiring large nonlinearities that are currently difficult to achieve.

An alternate approach was developed by Knill, Laflamme and Milburn (KLM) [3], who proposed using measurement to effect entangling interactions between optical qubits. Using this idea, KLM developed a scheme for scalable quantum computation based on linear optical elements, together with high-efficiency photodetection, feed-forward of measurement results, and single-photon generation. KLM thus showed that scalable optical quantum computation is in principle possible. Experimental demonstrations [4, 5, 6, 7, 8] of several of the basic elements of KLM have been achieved.

Despite these successes, the obstacles to fully scalable optical quantum computation with KLM remain formidable. The biggest challenge is to perform a two-qubit entangling gate in the near-deterministic fashion required for scalable quantum computation. KLM propose an ingenious scheme showing that this is possible in principle, but with a considerable overhead: doing a single entangling gate with high probability of success requires tens of thousands of optical elements. Several proposals (e.g., [9, 10]) have been made to reduce this overhead, but it still remains formidable even in these improved schemes.

A recent proposal [11] (c.f. [12]) combines the basic el-

ements of KLM with the cluster-state model of quantum computation [13] to achieve a reduction in complexity of many orders of magnitude. This scheme has been further simplified in [14], where it is estimated that only tens of optical elements will be required to implement a single logical gate. The resulting proposal for optical cluster-state quantum computing thus appears to offer an extremely promising approach to quantum computation. Recent experiments [15] have demonstrated the construction of simple optical cluster states. A recent review of work on optical quantum computation, including cluster-based approaches is [16].

While the optical cluster-state proposals [11, 14] present encouraging progress, for them to be considered credible approaches to fully scalable quantum computation, it is necessary to consider the effects of noise. In particular, it is necessary to establish a *noise threshold theorem* for the optical cluster-state proposals. A noise threshold theorem proves the existence of a constant *noise threshold* value, such that provided the amount of noise per elementary operation is below this level, it is possible to efficiently simulate a quantum computation of arbitrary length, to arbitrary accuracy, using appropriate error-correction techniques. In the standard quantum circuit model of computation such a threshold has been known to exist since the mid-1990s (see Chapter 10 of [17] for an introduction and references). However, the optical cluster-state proposals are not based on the circuit model, but rather on the cluster-state model of computation, and thus *a priori* it is not obvious that a similar noise threshold need hold.

Fortunately, recent work [18, 19, 20, 21] has shown that the fault-tolerance techniques developed for the circuit model can be adapted for use in the cluster-state model, and used to prove the existence of a *noise threshold* for noisy cluster-state computing. The earliest work [18, 19] established the *existence* of a threshold for clusters, without obtaining a value. [20] argued that in a specific noise model, the cluster threshold is no more than an order of magnitude lower than the threshold for circuits. The

*Electronic address: HLH@physics.uq.edu.au

†<http://www.qinfo.org/people/nielsen/blog/>

most recent work [21] combines ideas from cluster-state computing with topological error-correction to obtain a cluster threshold. However, neither [20] nor [21] are of direct relevance to the optical cluster-state proposal, since they make use of deterministic entangling gates, which are not available in linear optics, and the noise model does not include any process analogous to photon loss.

The present paper studies in detail the value of the noise threshold for optical cluster state computing. We use numerical simulations to estimate the threshold for a particular fault-tolerant protocol, for two different quantum codes. The paper is an extended version of an earlier work [22], which provided an overview (but few details) of the protocol and simulation techniques used, and only a brief summary of results.

Our threshold analysis is tailored to the dominant sources of noise in optical implementations of quantum computing. In particular, our simulations involve three different sources of noise: (a) the inherent nondeterminism of the entangling gates used to build up the cluster; (b) photon loss; and (c) depolarizing noise. The strength of noise source (a) is regarded as essentially fixed, while the strengths of (b) and (c) are regarded as variables that can be changed by improved engineering. Note that most existing work on thresholds (e.g., [20, 21, 23, 24]) in either clusters or circuits focuses on abstract noise models based on depolarizing noise, and neglects sources (a) and (b).

Noise sources (a) and (b) likely dominate actual experiments, and our protocol attempts to cope with these very efficiently. The protocols for decoding and correction can be made to take advantage of the knowledge the experimenter has of the locations of error types (a) and (b). For example, the well-known Steane 7-qubit code is usually used to correct a depolarization error on a single qubit. A more efficient use of the code is possible, in which it is used to correct photon loss or nondeterministic gate failure errors on as many as *two* qubits.

Although noise sources (a) and (b) will dominate, sources of noise other than (a) and (b) will also be present in experiments, and so it is important that our fault-tolerant protocol and analysis also deals with those. This is why we include noise source (c), as a proxy for all additional noise effects. Of course, in practice it is unlikely that depolarizing noise will be a particularly good model for the other noise sources. However, standard results in the theory of fault-tolerance imply that the ability to correct depolarizing noise implies the ability to correct essentially all reasonable physical noise models, and so depolarization is a good proxy for those other effects.

A prior work [25] (c.f. [26]) has calculated a threshold for optical quantum computation when the only source of noise is photon loss. In real experiments noise sources other than photon loss are present, such as dephasing, and protocols such as [25, 26] will amplify the effects of such noise at the encoded level. Thus, even if the original noise strength is very weak, encoding may amplify the noise to the point where it dominates the com-

putation. By contrast, our protocol protects against both photon loss and depolarizing noise, and by standard fault-tolerance results thus automatically protects against arbitrary local noise, including dephasing (in any basis), amplitude damping, etc.

Because our model includes multiple noise parameters, we do not obtain a single value for the threshold, as in most earlier work. Instead, we obtain a threshold *region* of noise parameters for which scalable quantum computing is possible. The main outcome of our paper is a series of threshold regions, with the different regions corresponding to varying assumptions regarding the relative noise strength of quantum memory, and the use of different quantum error-correcting codes. Qualitatively, we find that our fault-tolerant protocols are substantially more resistant to photon loss noise than they are to depolarizing noise, with threshold values of approximately 6×10^{-3} for photon loss noise (in the limit of zero depolarization noise), and 3×10^{-4} for depolarizing noise (in the limit of no photon loss). When both types of noise are present in the system, a typical value in the threshold region has a strength of 3×10^{-3} for photon loss noise, and a depolarization probability of 10^{-4} .

Our fault-tolerant protocol involves a number of innovations in addition to those already described, including: (1) the development of special techniques to deal with the inherent non-determinism of the entangling optical gates; (2) heavy use of the ability to parallelize cluster-state computations [27], and the ability to do as much of the computation off-line as possible; and (3) as a special case of the previous point, we develop a new method for doing fault-tolerant syndrome measurement which we call *telecorrection*. This has the striking property that repeated measurements of the syndrome are *guaranteed to agree* (which helps increase the threshold), unlike in standard protocols, where measurements only sometimes agree.

The structure of the paper is as follows. In Section II we briefly overview the required background on cluster-state computation and the optical cluster-state proposal. Section III describes our assumptions about the physical setting: what physical resources we are allowed, what quantum gates we can perform, and what noise is present in the system. Section IV describes briefly how we simulate noisy cluster-state computations. This is a surprisingly subtle topic, due to the multiple noise sources in our model, which is why it merits a separate section. Section V describes the details of the fault-tolerant protocol that we simulate, and presents the results of our simulations, including threshold regions for two different quantum codes. Section VI concludes.

II. BACKGROUND

In this section we introduce the required background on cluster states (Subsection II A), and optical cluster-state computation (Subsection II B). The main purpose

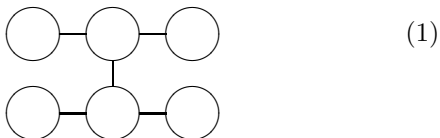
is to fix notation and nomenclature, and the reader looking for a more detailed introduction to these topics is referred to, e.g., [27, 28] for cluster states, and to [11, 14] for optical cluster-state computation.

A. Cluster-state computation

In this subsection we explain the cluster-state model of computation, and how it can be used to simulate quantum circuits. (By “simulate” in this context, we are referring to a procedure for converting a quantum circuit to an equivalent cluster-state computation). We give a rather in-depth treatment of the simulation procedure here, as our later discussion of fault-tolerance depends heavily on a thorough understanding of the details of this procedure. The presentation in this subsection is based on the treatments in [18, 28], which in turn are based on [13, 27]. The reader is referred to [18, 27] for proofs and a more in-depth discussion.

We begin by explaining the cluster-state model itself, initially ignoring the question of how a cluster-state computation can be used to simulate a quantum circuit. Broadly speaking, a cluster-state computation involves three steps: (1) the preparation of a special entangled many-qubit quantum state known as a *cluster state*; (2) an adaptive sequence of single-qubit measurements processing the cluster qubits; and (3) read-out of the computation’s result from the remaining cluster qubits. We now describe each step in detail.

The term “cluster state” refers not to a single quantum state, but rather to a family of quantum states. The idea is that an n -qubit cluster state is specified by a graph on n vertices; to each vertex we associate a corresponding qubit in the cluster, and we apply a graph-dependent preparation procedure to the qubits in order to define the cluster (as described below). For example, the following graph represents a six-qubit cluster:



The cluster state associated to such a graph may be defined as the result of applying the following two-stage preparation procedure:

1. Prepare each of the n qubits in the state $|+\rangle \equiv (|0\rangle + |1\rangle)/\sqrt{2}$.
2. Apply CPHASE (controlled-PHASE) gates between cluster qubits whose corresponding graph vertices are connected by an edge.

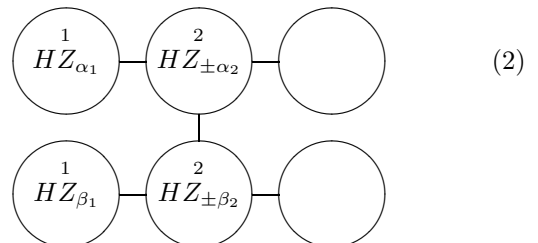
Although we have not specified the order in which the CPHASE gates in the second step are to be applied, this is okay, because these gates all commute. Note also that although this preparation procedure defines the cluster

state associated to the graph, it is of course possible to use other preparation procedures to prepare the same state. (An important case in point is discussed in the next subsection – how the so-called fusion gate may be used to prepare optical cluster states).

Once the cluster is prepared, the next step in a cluster-state computation is to perform a sequence of processing measurements on the cluster. These measurements are single-qubit measurements, whose location and nature may depend (via a polynomial-size classical computation) on the outcome of earlier measurements.

The output of the cluster-state computation, just before the final readout, consists of (a) the quantum state $|\psi\rangle$ of the qubits remaining after completion of the processing measurements, and (b) the sequence of classical measurement outcomes obtained during processing, which we denote \mathbf{c} . These classical measurement outcomes will generally affect the way in which we interpret the quantum state output from the computation. In particular, it is convenient to regard the output as being the state $\sigma_{\mathbf{c}}|\psi\rangle$, where $\sigma_{\mathbf{c}}$ is an n -qubit product of Pauli matrices which is some suitable function of the bit string \mathbf{c} .

It is often convenient to have a graphical representation of a cluster-state computation. For this purpose we use notation along the following lines:



The overall shape of the diagram denotes the graph state to be created at the beginning of the computation. Labels indicate qubits on which processing measurements occur, while unlabeled qubits are those which remain as the output of the computation when the processing measurements are complete. Note that qubits are labeled by a positive integer k and a single-qubit unitary, which we refer to generically as U . Here $U = HZ_{\pm\alpha_j}, HZ_{\pm\beta_j}$. The k label indicates the time order in which processing measurements are to be performed. Qubits with the same label are allowed to be measured in any order relative to each other, or simultaneously. Time-ordering is important, because some measurement results need to be fed-forward to control later measurement bases. The U label is used to specify the basis in which the qubit is measured, indicating that the measurement may be performed by applying the unitary U , and then performing a computational basis measurement. (This is equivalent to performing a measurement in the $\{U^\dagger|0\rangle, U^\dagger|1\rangle\}$ basis.) The \pm notation in $HZ_{\pm\alpha_2}$ and $HZ_{\pm\beta_2}$ indicates that the choice of sign depends on the outcomes of earlier measurements, in a manner that needs to be specified separately. Details of how this choice should be made are

given later in this subsection, and further examples can be found in, e.g., [18].

We now describe a recipe that may be used to convert a quantum circuit to a cluster-state computation. As part of this recipe we will introduce the notion of a *Pauli frame*. Initially the Pauli frame will appear to be merely a bookkeeping device, but in our later description of noisy cluster-state computation it will be an important tool for tracking the effects of noise.

The key to simulating quantum circuits with cluster states is the following circuit identity ([29], see also [28]):

$$\begin{array}{c} |\psi\rangle \\ |+\rangle \end{array} \begin{array}{c} \bullet \\ \bullet \end{array} \begin{array}{c} \boxed{HZ_\theta} \\ \text{---} \end{array} \begin{array}{c} \boxed{\text{meter}} \\ \text{---} \end{array} \begin{array}{c} = m \\ \text{---} \end{array} \quad (3)$$

$X^m HZ_\theta |\psi\rangle$

Note that the measurement basis is the computational basis, and $m = 0, 1$ is the measurement outcome. We shall call this circuit the *transport circuit*, since its effect is to transport (and simultaneously transform) the quantum information input onto the second qubit.

We will explain how to use cluster states to simulate quantum circuits through a series of examples, starting with the following two-gate single-qubit circuit:

$$|+\rangle \text{---} \boxed{HZ_{\alpha_1}} \text{---} \boxed{HZ_{\alpha_2}} \text{---} \quad (4)$$

Note that we assume the qubit starts in the $|+\rangle$ state, and that single-qubit gates are of the form HZ_α . Later we will show how to simulate multi-qubit circuits involving the CPHASE. Jointly, these operations are universal for computation, and so the ability to simulate them is sufficient to simulate an arbitrary quantum circuit.

The cluster-state computation used to simulate Circuit (4) is:

$$\begin{array}{c} \textcircled{1} \\ HZ_{\alpha_1} \end{array} \text{---} \begin{array}{c} \textcircled{2} \\ HZ_{\pm\alpha_2} \end{array} \text{---} \textcircled{} \quad (5)$$

By definition, this cluster-state computation has an output equal to the output of the following quantum circuit¹:

$$\begin{array}{c} |+\rangle \\ |+\rangle \\ |+\rangle \end{array} \begin{array}{c} \bullet \\ \bullet \\ \bullet \end{array} \begin{array}{c} \boxed{HZ_{\alpha_1}} \\ \text{---} \end{array} \begin{array}{c} \boxed{\text{meter}} \\ \text{---} \end{array} \begin{array}{c} \text{---} \\ \text{---} \end{array} \begin{array}{c} \boxed{HZ_{\pm\alpha_2}} \\ \text{---} \end{array} \begin{array}{c} \boxed{\text{meter}} \\ \text{---} \end{array} \quad (6)$$

¹ Note that the double vertical lines emanating from the meter on the top qubit indicate classical feed-forward and control of later operations.

In this circuit we have measured the first qubit *before* doing the CPHASE between the second and third qubits used during creation of the cluster. This does not change the output since these operations are on different qubits, and thus commute. We do this because it enables us to understand the output as the result of two cascaded circuits of the form of (3), as indicated by the highlighted boxes.

It will be helpful to consider the quantum state of the qubits at each of three intermediate locations. The first location is the initial state of the first qubit, i.e., $|+\rangle$. Note that this is exactly equal to the input for Circuit (4).

The second location is the state of the second qubit output by the first of the transport circuits and used as input to the second transport circuit. This state is $X^{m_1} HZ_{\alpha_1} |+\rangle$, where m_1 is the output of the first measurement. This is equal to the state of the qubit in Circuit (4) after the first gate, up to the known Pauli matrix X^{m_1} . We will see shortly that we can compensate for this known Pauli matrix by a suitable choice of the sign in $\pm\alpha_2$.

The third location is the state of the third qubit after both transport circuits, i.e., at the end of the computation. This state is $X^{m_2} HZ_{\pm\alpha_2} X^{m_1} HZ_{\alpha_1} |+\rangle$, where m_2 is the output of the measurement on the second qubit. By choosing the sign of $\pm\alpha_2$ so that $Z_{\pm\alpha_2} X^{m_1} = X^{m_1} Z_{\alpha_2}$, and using the identity $HX^{m_1} = Z^{m_1}H$, the output may be rewritten as $X^{m_2} Z^{m_1} HZ_{\alpha_2} HZ_{\alpha_1} |+\rangle$. Up to the known Pauli matrix $X^{m_2} Z^{m_1}$, which can be compensated in post-processing, this is identical to the output of the single-qubit circuit (4).

The presence of these known Pauli matrices motivates us to define the notion of a *Pauli frame* for the cluster-state computation (5), as follows. At the beginning of the computation, the Pauli frame is just the product $I \otimes I \otimes I$ on three qubits. We measure the first qubit, with output m_1 , and the updated Pauli frame is the two-qubit operator $X^{m_1} \otimes I$. We measure the second qubit, and the updated Pauli frame is the single-qubit operator $X^{m_2} Z^{m_1}$. Thus, at each stage the Pauli frame relates the state actually input to the remaining stages of the cluster-state computation to the ideal state of the circuit being simulated.

In general, suppose we are using a horizontal cluster to simulate an arbitrary single-qubit computation. Then by definition the initial Pauli frame is just the tensor product of identities on all cluster qubits. Suppose at some stage we have a Pauli frame which is $X^x Z^z$ on the first remaining cluster qubit, and acts as the identity on all other qubits. After measuring the first remaining cluster qubit, and obtaining the result m , the updated Pauli frame is $X^{z+m} Z^x$ on the first remaining qubit after measurement, and the identity on all the other qubits.

The Pauli frame is determined by the measurement results, and thus will always be known to an experimenter observing the computation. Furthermore, the Pauli frame determines the basis in which later measurements are performed. As the example above shows, if the

Pauli frame is $X^x Z^z$ on the qubit to be measured, then the measurement basis to simulate a HZ_α gate is $HZ_{+\alpha}$ if $x = 0$, and $HZ_{-\alpha}$ if $x = 1$.

The reader may wonder why we carry all the extra identity terms around in the Pauli frame, since they aren't explicitly used. Later we will see that keeping these terms is quite useful in the analysis of noisy cluster-state computations.

Let's generalize these ideas to the simulation of multi-qubit quantum circuits. Consider the following example, which illustrates the general ideas:

$$\begin{array}{c} |+\rangle \text{---} [HZ_{\alpha_1}] \text{---} \bullet \text{---} [HZ_{\alpha_2}] \text{---} \\ |+\rangle \text{---} [HZ_{\beta_1}] \text{---} \bullet \text{---} [HZ_{\beta_2}] \text{---} \end{array} \quad (7)$$

This can be simulated using the cluster-state computation of (2). The correspondence between the two is as follows. Each qubit in the quantum circuit is replaced by a horizontal row of cluster qubits. As in the single-qubit case, different horizontal qubits in the cluster represent the original circuit qubit at different times, with each gate HZ_α replaced by a single qubit in the cluster. CPHASE gates in the quantum circuit are simulated using a vertical “bridge” connecting the appropriate cluster qubits in different rows.

As in the earlier example, at any given stage of the cluster-state computation we define a Pauli frame which is a product of Pauli operators on the remaining cluster qubits. Initially, this is the identity on all six cluster qubits. Consider the measurement on the two leftmost qubits. In each case, the rule for updating the Pauli frame is exactly as described earlier. The only difference arises when the qubit being measured has a vertical bond. In this case, suppose prior to the measurement the Pauli frame has entry $X^{x_1} Z^{z_1}$ on the qubit being measured, and entry $X^{x_2} Z^{z_2}$ on the qubit attached via the vertical bond. The update rule for after the measurement is in two steps: (1) replace the Pauli frame on these two qubits by $X^{x_1} Z^{z_1+x_2}$ and $X^{x_2} Z^{z_2+x_1}$, respectively; (2) apply the earlier rules for horizontally attached qubits, just as though the vertical bond was not present.

A generalization of the earlier analysis for the single qubit case shows that with these rules, the state at the end of the cluster-state computation is equal to the product of the Pauli frame with the output from the quantum circuit being simulated. Since the Pauli frame is known by the experimenter, its presence can be compensated in post-processing, and the two types of computation are equivalent.

We have described our simulations of circuits by a cluster-state computation where the measurements are done left-to-right on the qubits. In fact, as emphasized in [27], when the operations being simulated are Clifford group operations, no measurement feed-forward is required, and it is possible to change the order in which measurements are done. In particular “later” parts of the quantum circuit can be simulated earlier during the

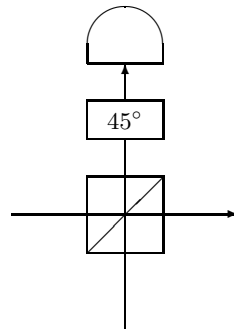


FIG. 1: The fusion gate. Two optical modes are combined on a polarizing beam splitter, which reflects vertically polarized light only. The polarization of one mode is then rotated through 45° , before being measured using a polarization discriminating photon counter.

cluster-state computation. This means it is possible to *parallelize* operations that would be done at different times in the circuit model, and even in some instances to *premeasure* parts of the cluster. We will make heavy use of these ideas in our fault-tolerant protocol, which consists entirely of Clifford group operations. Note however, that even in the cases where qubits may be measured out of order, the update rules for the Pauli frame should be applied as though measurements were done in the conventional left-to-right order.

B. Optical cluster-state computation

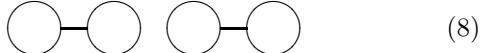
We've described cluster-state computation as an abstract model of quantum computation. We now discuss how cluster-state computation can be implemented optically. The method we use is a variant of [14], with key ideas coming from [11] and [3].

In this model, qubits are encoded in two optical polarizations (horizontal H and vertical V) corresponding to a single spatial mode. We will build up clusters using a supply of Bell states, $(|HH\rangle + |VV\rangle)/\sqrt{2}$, and a gate known as the *fusion gate*, which is illustrated in Fig. 1. Combining the ability to build up clusters with linear optics (used to effect single-qubit rotations) and a polarization discriminating photon counter, this thus enables quantum computing. Note that [14] uses two variants of the fusion gate; we will only make use of one of these gates, and so refer to it simply as *the* fusion gate.

To see how this works, suppose a fusion gate is applied to two cluster qubits that are not connected by an edge. Then provided a single photon is registered at the output (either horizontally or vertically polarized), it can be shown the resulting quantum state is a cluster state in which the two qubits have been *fused*, i.e., combined into a single cluster qubit whose edge set contains all the edges of both fused qubits. This occurs with probability 50 percent, and we say that the fusion gate has been

successful when it happens. By contrast, if zero or two photons register at the output, then the fusion gate has failed, and it can be shown that the effect is to delete the two qubits from the cluster. Failure occurs with probability 50 percent.

Using Bell states and fusion gates we can efficiently build up large clusters. The basic idea can be understood from the following example of how to build up a linear cluster, following [14]. Note that the Bell state is simply a two-qubit cluster state, up to unimportant local unitaries, and so we can prepare a pair of two-qubit clusters:



Successful fusion of a qubit from one Bell pair with a qubit from the other Bell pair results in the three-qubit linear cluster:



If this fails we can try again from scratch. Using this procedure, we can obtain a supply of three-qubit linear clusters, with the average cost of preparation a small constant. Using such three-qubit linear clusters as a resource, we can build up longer linear chains by attempting to fuse three-qubit linear clusters onto the end of an existing chain. With probability 50 percent this succeeds, adding two qubits to the chain. With probability 50 percent it fails, resulting in the loss of a qubit from the chain. Thus, on average one qubit is added to the chain, and standard results about random walks imply that it is possible to build up a long linear chain with only a small constant overhead.

More complex clusters can be built up using similar ideas. To achieve good thresholds, it's important to design the best possible procedures for building up clusters. This is a complex task, trading off two opposing desiderata: (1) the need to keep the cluster generation near-deterministic, which is most easily accomplished by preparing large numbers of cluster qubits well in advance of when they are measured (c.f. [11]), and (2) the fact that qubits left to themselves tend to decay due to noise. As a result, the exact procedure we use to build up clusters in our fault-tolerant protocol is rather involved, and we defer a detailed discussion until later in the paper.

III. PHYSICAL SETTING

In this section we describe in detail both what physical operations we assume can be done, and our model of noise.

Physical operations: We assume the following basic elements are available. First, a source of polarization-entangled Bell pairs (specifically, the state $[|0\rangle \otimes (|0\rangle + |1\rangle) + |1\rangle \otimes (|0\rangle - |1\rangle)]/2$ in qubit notation). Physically, these can be produced in a number of different ways,

but the details don't matter to our analysis. Second, single-qubit gates can be performed on the optical qubits. Physically, this can be done using linear optics, following KLM. Third, the fusion gate of Browne and Rudolph can be applied. Fourth, efficient polarization-discriminating photon counters capable of distinguishing 0, 1 and 2 photons are available. These can be used to effect measurements in the computational basis, and are also used to verify the success or failure of the fusion gate. Note that having single-qubit gates and computational basis measurements allows us to effect single-qubit measurements in an arbitrary basis. Single-qubit gates do not appear explicitly in our protocol, rather only as part of single-qubit measurements.

Implicit in our discussion up to now is the concept of a *time step*. For simplicity, assume that all the basic elements take the same amount of time, and we describe our circuit in terms of a sequence of such time steps. As a consequence, an important additional element that must be available is the quantum memory “gate”, during which an optical qubit ideally does nothing for a time step, but may still be affected by noise. Physically, it's not yet clear what the best way of implementing such a quantum memory will be.

We've described the basic elements in our model of quantum computation. However, a number of important additional assumptions are made about how these elements can be put together. First, we assume that any two qubits can be interacted directly. This is reasonable, given the ease of moving photonic qubits from one location to another. Second, we assume the ability to perform operations on all the qubits in parallel. Third, we assume the availability of classical computation, communication, and feed-forward, all on a timescale fast compared with the unit time step. The feed-forward requirement is particularly demanding, since it requires us to decide which qubits interact in a time-step, based on the results of measurements in the previous time-step. To some extent, this requirement is imposed merely to simplify our simulations, and it seems likely that the requirement can be relaxed, but this remains a topic for further investigation.

Noise model: We now describe our model of the physical sources of noise. As stated in the introduction, our protocol deals with three kinds of noise: (a) the inherent nondeterminism of the fusion gates; (b) photon loss; and (c) depolarizing noise. We now describe these in more detail.

In the last section we already described the noise due to the inherent non-determinism of the fusion gate: with probability 50% the gate succeeds, and fusion is effected, while with probability 50% it fails, and the two qubits are measured in the computational basis.

We assume a single parameter γ controls the strength of the photon loss. γ is the probability per qubit per time step of a photon being lost. We assume this probability is independent of the state of the qubit, and that photon loss affects every basic operation in our protocol, as

follows:

- Bell-state preparation: After the state has been prepared, each of the two qubits independently experiences photon loss with probability γ .
- Memory, single-qubit, and fusion gates: Before the gate each input qubit experiences photon loss with probability γ . In the case of the fusion gate, which has two inputs, we assume the loss probabilities are independent. Later in the paper we also investigate the case where the photon loss rate for memory gates has been suppressed relative to the other gates.
- Measurement: Before measurement we assume photon loss occurs with probability γ . Physically, this can model both the loss of photons from the relevant optical modes, and also detector inefficiencies.

It is worth noting that detector inefficiencies are currently much worse than other sources of photon loss, and it could be argued that detector inefficiency and other photon loss rates should be treated as independent parameters (or, alternately, that all other photon loss rates be set to zero). However, it is clear that turning off or turning down photon loss noise in locations other than before measurement can only improve the threshold, and so we have used the more pessimistic model described above. In fact, it can be shown that photon loss occurring in locations other than before measurements propagates to become equivalent to photon loss before measurements. Thus, the model in which photon loss occurs only before measurement should have a threshold for photon loss noise several times higher than the results we report in this paper.

Note also that we have chosen a model of photon loss during Bell-state preparation that acts independently on each qubit in the pair. It would perhaps be more physically realistic for loss to occur in a manner that is highly correlated between the two qubits in the Bell pair (i.e., making it more likely that both photons in the pair are lost as opposed to just one). However, the design of our fault-tolerant protocol ensures that we can always detect situations where both photons in a Bell state are lost, and thus this type of coincidental loss has no negative effect on the threshold. So, our choice of uncorrelated photon loss is the more pessimistic of the two alternatives.

Similarly to photon loss, we assume a single *depolarizing parameter* ϵ controls the strength of the depolarizing noise. We assume depolarization affects every basic operation, as follows:

- Bell-state preparation: After the state has been prepared, the joint state of the two qubits is depolarized as follows: with probability $1 - \epsilon$ nothing happens, while with respective probabilities $\epsilon/15$ we apply each of the 15 non-identity Pauli product operators IX, XX etcetera.

- Memory and single-qubit gates: Before each gate we depolarize as follows: with probability $1 - \epsilon$ nothing happens, while with respective probabilities $\epsilon/3$ we apply each of the 3 non-identity Pauli operators X, Y and Z .
- Fusion gate: The joint state of the two qubits is depolarized with parameter ϵ (in the same way as described for Bell-state preparation above) before being input to the gate.
- Measurement: Before measurement the qubit is depolarized with parameter ϵ (in the same way as described for memory and single-qubit gates above).

Note that in our noise model noise occurs before or after operations. In a real physical setting, noise will also occur during gate operations. However, standard fault-tolerance techniques (see, e.g., [30]) can be used to show that noise during an operation can be regarded as completely equivalent to noise before or after that operation.

The noise model we have described is obviously an approximation to reality, and is incomplete in various ways. For example, it is difficult to justify on physical grounds using the same two noise strength parameters for all operation types. Also, additional noise sources that may have an effect in real implementations include dark counts, dephasing, and non-local correlations. However, it can be shown that the fault-tolerant protocol we implement automatically provides protection against such noise sources. We haven't done a detailed investigation of the threshold for these noise sources, or for the case of different noise strengths for different operation types, but believe that the results would be in qualitative agreement with the results of the present paper.

IV. HOW WE SIMULATE A NOISY CLUSTER-STATE COMPUTATION

In this section we explain how to simulate a noisy cluster-state computation. We don't yet describe the details of the fault-tolerant protocol, leaving those to the next section. However, the protocol is simulated using essentially the techniques we now describe.

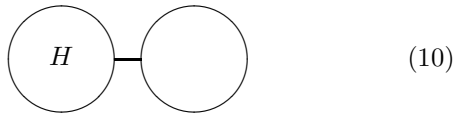
We concentrate on the case when the errors are solely Pauli-type errors. It turns out that a simple modification of the techniques used to describe these errors can be used to describe the non-deterministic failure of fusion gates, or photon loss. However, we defer this discussion to the next section as it depends on some details of the fault-tolerant protocol.

A. Example

We begin with a toy example of a noisy cluster-state computation in which noise is introduced at just a single location, and we study how this affects the remainder of

the computation. This example will motivate our later abstractions and the data structures used to model noise.

The example is a two-qubit cluster-state computation:



We imagine that the two qubits of the cluster are perfectly prepared. After preparation, we suppose a single Pauli Z error corrupts the first qubit, so the actual physical state of the cluster is related to the ideal state by an overall error $Z \otimes I$. Now we suppose a perfect H operation and computational basis measurement is carried out on the first qubit, yielding an outcome $m = 0$ or 1 . It will be convenient to regard the combined Hadamard and measurement as a single operation, a perfect measurement in the X basis. This completes our example computation.

At the end of the computation, the experimenter believes the resulting state of the second qubit is $X^m H|+\rangle$. However, a calculation shows that the actual state is $X^{m+1} H|+\rangle$. Mathematically, there are two different ways we can think about this resulting state:

- Measurement of the first qubit propagates the Z error on that qubit to the second qubit, and causes it to become a physical X error on that qubit.
- Measurement of the first qubit causes the Z error on that qubit to turn into an X error in the Pauli frame of the second qubit, but eliminates all physical errors.

While these points of view are equivalent, we will take the second point of view, as it turns out that in more complex examples, it is this point of view which gives the simplest description of what is going on.

This analysis can be repeated for the case where, instead of a Z error, we had a single X error occur on the first qubit. However, this case is more trivial, because the X error followed by the perfect X basis measurement is equivalent to a perfect X basis measurement alone, and thus the resulting state is $X^m H|+\rangle$, as expected by the experimenter. Thus, in this case the effect of measurement is simply to eliminate the physical error.

B. General description of the introduction and propagation of Pauli noise

Our simulations of Pauli noise in cluster-state computation are based on generalizations of the concepts introduced in the previous example. There are two basic data structures that we keep track of. The first is the *physical error* in the state of the cluster. This is a tensor product of Pauli matrices, one for each cluster qubit. This begins as the identity at every qubit, and we will describe below how it is modified as noise and gate operations occur.

The second data structure is the *error in the Pauli frame* of the cluster. Again, this is a tensor product of Pauli matrices, one for each qubit in the cluster. It begins as the identity at every qubit, and will be modified during the simulation according to rules described below.

It is notable that our description of noisy cluster-state computation is thus based entirely on products of Pauli operators. What makes this description possible is that all the operations we simulate are Clifford-group operations, and this ensures that the errors remain Pauli errors at all times. It is also worth noting that in our simulations we do not keep track of the actual state of the cluster, nor of the Pauli frame, but only of the errors in each. This is because the aim of our fault-tolerance simulations is to determine various statistics associated to these errors, and the actual state of the cluster is not of direct importance.

Note that in our description, physical errors and Pauli frame errors are not generally interchangeable, since they undergo different propagation rules (described later in this subsection) and thus may have different effects on the final state of the computation. Errors in the Pauli frame are introduced only as a result of noise-affected measurements in transport circuits, and propagate as a result of the Pauli frame update rules (described in Subsection II A) that the experimenter applies. Physical errors describe noise on the state itself, and propagate according to how the Pauli matrices commute through the various quantum operations performed on the state.

As we have described, the physical error and Pauli frame error are products of Pauli operators on all the remaining cluster qubits. It is often convenient to focus on one or just a few cluster qubits rather than the entirety. For this purpose we will refer to *local physical errors* and *local Pauli frame errors*, which are just the corresponding Pauli operators for a specified qubit or qubits. It will also be convenient to describe such local errors either in matrix form as $X^x Z^z$, or in terms of the pair (x, z) , and we will use these descriptions interchangeably. So, for example, we may refer to either X^x or simply x as the X error. We will routinely ignore global phase factors in our description of errors, so, e.g., XZ and ZX are regarded as equivalent.

The final concept needed to explain the way we update our data structures is that of a *terminating qubit*. We define a cluster qubit to be terminating if it has no horizontal bonds. It may or may not have vertical bonds. For example, in a horizontal cluster being used to simulate a single-qubit computation, the qubit at the rightmost end of the cluster becomes a terminating qubit after all the other qubits have been measured. The significance of terminating qubits in a cluster-state computation is that measurement of these qubits reveals the outcomes of the computation. By contrast, measurement of non-terminating qubits merely reveals information which can be used to propagate quantum information to other parts of the cluster.

We now describe the rules for updating both our data

structures for each of the possible operations that can occur during a noisy cluster-state computation.

Update rule for depolarization event: The physical error is updated by matrix multiplication by the appropriate randomly-chosen error (e.g., X, Y or Z). The error in the Pauli frame is not affected.

Update rule when a non-terminating qubit is measured in the X basis: It is easiest to describe this by describing two separate cases: the case when there is a single horizontal bond attached to the qubit being measured, to the right; and the case where both vertical and horizontal bonds are present.

Suppose the qubit being measured has a single horizontal bond attached, to the right. Suppose before the measurement the local physical error on the qubit being measured is $X^{x_{1p}}Z^{z_{1p}}$, and the local Pauli frame error is $X^{x_{1f}}Z^{z_{1f}}$. Suppose the corresponding values for the qubit on the right are $X^{x_{2p}}Z^{z_{2p}}$ and $X^{x_{2f}}Z^{z_{2f}}$. After the measurement the updated values for the local physical and Pauli frame errors of the qubit on the right are as follows:

$$x'_{2p} = x_{2p} \quad (11)$$

$$z'_{2p} = z_{2p} \quad (12)$$

$$x'_{2f} = x_{2f} + z_{1p} + z_{1f} \quad (13)$$

$$z'_{2f} = z_{2f} + x_{1f}. \quad (14)$$

These rules are derived from our earlier description of the transport circuit and the rules for updating the Pauli frame, along essentially the same lines as the example in Subsec. IV A. As in the example, we see that X physical errors on the qubit being measured are eliminated, and Z physical errors propagate to become X errors in the Pauli frame. Similar reasoning shows that X errors in the Pauli frame of the qubit being measured propagate to become Z errors in the Pauli frame of the attached qubit, and vice versa for Z errors in the Pauli frame.

Suppose the qubit being measured has a vertical bond, and a rightward horizontal bond. Suppose we label the qubits 1 (qubit being measured), 2 (qubit to the right), and 3 (qubit attached by vertical bond). We will denote the values for the local physical error and local Pauli frame error by x_{jp}, z_{jp} and x_{jf}, z_{jf} , respectively, where j labels the qubit. We update these in two stages, with the update method derived from the two stages for updating the Pauli frame when a vertical bond is present, as described in Subsec. II A. The first stage is associated

to the vertical bond. We set:

$$x'_{1p} = x_{1p} \quad (15)$$

$$z'_{1p} = z_{1p} \quad (16)$$

$$x'_{1f} = x_{1f} \quad (17)$$

$$z'_{1f} = z_{1f} + x_{3f} \quad (18)$$

$$x'_{3p} = x_{3p} \quad (19)$$

$$z'_{3p} = z_{3p} \quad (20)$$

$$x'_{3f} = x_{3f} \quad (21)$$

$$z'_{3f} = z_{3f} + x_{1f}. \quad (22)$$

The local physical and Pauli frame errors for qubit 2 are not changed during this step. For the second stage we behave as though the vertical bond has been deleted, and use our new values for the physical and Pauli frame errors as input to the update rules for the case of a horizontal bond, Equations (11)-(14).

Update rule for measuring terminating qubits in the X basis: We first describe the update rules for the case when the terminating qubit has no vertical bonds attached. The update rule is to compute the *total error*, which we define as the product of the local physical and Pauli frame errors on that qubit. The qubit is then deleted from the cluster, and its local physical and Pauli frame errors are deleted from the corresponding data structures. The total error $X^x Z^z$ determines whether or not the measurement outcome (e.g., of syndrome information) contains an error. Since the measurement is in the X basis, the error in the measurement is simply z . The aim of our fault-tolerant simulations will be to determine various statistics associated to this total error.

Consider now the case when the terminating qubit has a vertical bond also, before being measured in the X basis. In this case we simply follow the rules of Equations (15)-(22) for updating the errors, and then treat the qubit as though the vertical bond has been deleted, and apply the rules described earlier for treating a terminating qubit.

Update rule for measuring a qubit in the Z basis: In our protocols we only ever do such a measurement on non-terminating qubits, and so restrict our attention to this case. In an ideal cluster-state computation the effect of a Z measurement with outcome $m = 0$ or 1 is effectively to remove that qubit from the cluster [13], and apply Z^m to all neighbouring qubits. An experimenter getting a result m can therefore update the Pauli frame of neighbouring qubits by multiplying each by an extra factor of Z^m .

To describe the update rule in this case, we define the total error to be $x_t = x_p + x_f, z_t = z_p + z_f$, where subscript ps denote physical errors, and subscript fs denote Pauli frame errors. The error in the measurement outcome will be x_t , since Z flips don't affect Z basis measurements. So the update rule is merely to discard the local physical and Pauli frame errors from our overall physical error and Pauli frame error, and to introduce an additional Z^{x_t} Pauli frame error on all neighbouring qubits.

Update rules for the fusion gate: We separate our analysis into cases when the fusion gate is unsuccessful and successful. When unsuccessful the fusion gate results in a Z basis measurement being applied to the qubits we are attempting to fuse. This case can be described by the rules stated above for Z basis measurements.

When the fusion gate is successful we update as follows. We label the qubits being fused as qubit 1 and 2. It turns out that in our fault-tolerant protocol we *never* fuse qubits which have Pauli frame errors. Thus we can assume that the initial errors on the qubits being fused are simply x_{jp}, z_{jp} , where $j = 1, 2$ labels the qubit. For distinctness we will call the physical and Pauli frame errors of the output qubit x_{3p} and z_{3p} ; the 3 is merely for clarity, and does not indicate the creation of a new physical qubit. The update rule is as follows:

- For each qubit neighbouring qubit 1, we add x_{2p} to the Z physical error.
- Vice versa, for each qubit neighbouring qubit 2, we add x_{1p} to the Z physical error.
- $x_{3p} = x_{1p} + x_{2p}$,
- $z_{3p} = z_{1p} + z_{2p}$.

These rules follow straightforwardly from the definition of the fusion gate.

V. FAULT-TOLERANT PROTOCOL

A. Introduction

In this section we describe in detail our fault-tolerant protocol, and the threshold results we obtain. We begin in this subsection with a brief discussion of the historical background and antecedents to our work. We begin describing the technical details of the protocol in the next subsection.

The basic theory of fault-tolerant error-correction originated in the mid-1990s, with the fault-tolerant constructions of Shor [31]. These constructions were used to prove a threshold theorem for quantum computation by Aharonov and Ben-Or [32, 33], Gottesman and Preskill (see, e.g., [34, 35, 36, 37, 38]), Kitaev [39], and Knill, Laflamme and Zurek [30]. This work established the *existence* of a threshold for a wide class of noise models, and gave pessimistic analytic bounds on the threshold, but did not establish the exact value of the threshold.

A large body of numerical work aimed at determining the threshold has since been done. Especially notable is the work by Steane [24], who did the first detailed numerical investigations of the threshold, and the recent work by Knill [23], who has established the best known thresholds in the standard quantum circuit model. Many of our techniques are based on those described by Steane. We will also see below that there is some overlap with the techniques of Knill. Of course, the very different nature

of optical cluster-state computation demands many new techniques, and care must be taken in comparing the values of thresholds in this model and the standard quantum circuit model.

As explained in the introduction, Nielsen and Dawson [18] proved the existence of a threshold for optical cluster-state computing (c.f. [19, 20, 21]). The basic idea of the construction in [18] is to show that if we take a quantum circuit, convert it into a fault-tolerant form using multiple layers of concatenated coding, and then simulate the circuit using optical cluster states, the resulting noisy optical cluster-state computation is itself fault-tolerant. This proof relied on an important theorem of Terhal and Burkard [40] establishing a threshold for non-Markovian noise in the standard circuit model.

When we began the work described in this paper, our intention was to apply the procedure described in [18] to a fault-tolerant circuit protocol similar to that considered by Steane [24]. In the event, our protocol involves substantial improvements over this basic procedure, is manifestly fault-tolerant, and gives a much better threshold. The improvements include: optimizing our treatment of photon loss and non-determinism; exploiting the ability to premeasure and parallelize parts of the cluster-state computation; and taking advantage of the ability to premeasure clusters in order to improve ancilla creation. All these improvements are described in detail below.

B. Broad picture of fault-tolerant protocol

In this subsection we outline our fault-tolerant protocol. The protocol is split into two main parts.

The first part is a cluster-based simulation of a variant of Steane's fault-tolerant protocol. We have modified Steane's protocol to deal with the non-deterministic nature of the optical gates, and introduced several cluster-based tricks to improve the threshold. This protocol and the results of our simulations are described in Subsection VC.

The second part is a deterministic gate-based protocol, whose purpose will be explained in the paragraphs below. This protocol is also based on Steane's methods, again with some substantial variations. This protocol and the results of our simulations are described in Subsection VD.

The reason for using the two protocols is that the actual cluster threshold is obtained by concatenating a single encoded level of the cluster protocol with multiple levels of the deterministic protocol. This works because our multiply concatenated fault-tolerant cluster protocol is equivalent to building up a fault-tolerant implementation through multiple levels of concatenation in the circuit model, and then replacing each gate in the bottom level by a clusterized equivalent.

To obtain the overall behaviour of such a protocol, it is not feasible to directly simulate the multiply concatenated computation. Instead, we do one simulation of the

clusterized protocol at just a single level of encoding, and another of the deterministic protocol, again at a single level of encoding. We then make an argument allowing us to use the data obtained from these two protocols to estimate the overall behaviour if multiple layers of concatenation had in fact been used. The details of how this is done are described in Subsection V E.

C. The cluster-based protocol

Our cluster-based protocol performs multiple rounds of clusterized quantum error-correction, effectively implementing a fault-tolerant quantum memory. Following previous numerical work on the threshold (e.g. [23, 24]) we do not simulate dynamical operations at the encoded level. However, our simulations could easily be varied to implement encoded Clifford group operations with a small additional overhead, and this will leave the threshold essentially unchanged. Computational universality requires at least one encoded non-Clifford group operation. This is difficult to simulate, and previous workers [24] have argued that it changes the threshold very little, since error-correction (which makes up the bulk of a fault-tolerant circuit) is done using only Clifford group operations.

Our simulations extract various statistics regarding failure modes of our fault-tolerant protocol. Thus we do multiple trials of the protocol in order to estimate these statistics. A single trial involves the simulation of multiple rounds of quantum error-correction applied to a single encoded logical qubit. This is all done within the optical cluster-state model of computation, with the noise model as described in Section III.

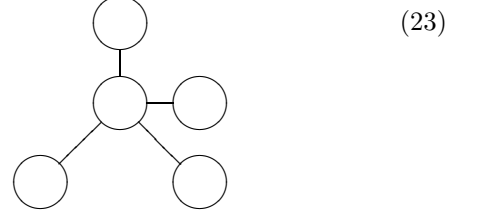
The major elements of a single trial are as follows: (1) the input state; (2) the input to a round of quantum error-correction; (3) the preparation of the ancilla states used to extract error syndromes; (4) the preparation and use of the *telecorrector* cluster enabling interactions between the encoded data and the ancilla; (5) the reduction of photon loss and non-determinism to Pauli-type errors; and (6) decoding.

We will now describe each of these elements in detail. First, however, we discuss some special tools which are used repeatedly in multiple elements of our cluster-state computation.

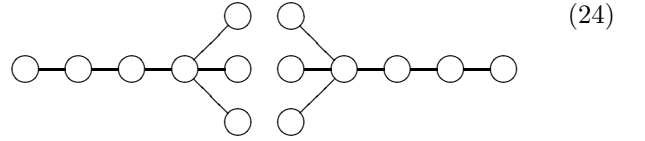
1. Tools for optical cluster-state computing: microclusters, parallel fusion, and postselection

Earlier in the paper we've described how to clusterize quantum circuits, and how to implement cluster-state computation optically. However there are three useful additional tools which we use repeatedly through the entire protocol, and which deserve special mention: *microclusters*, *parallel fusion*, and *postselection*.

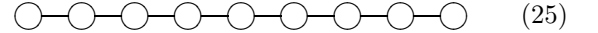
A microcluster is a star-shaped cluster, for example:



The central node in the microcluster is known as the *root node*, while the other nodes are *leaf nodes*. Microclusters are used as a tool to build up larger clusters. In particular, the use of microclusters ensures that these larger clusters always have multiple leaf nodes, which can be used to enhance the probability with which we fuse two larger clusters:



We can attempt three simultaneous fusion gates between adjacent leaf nodes of the two clusters. With a probability that goes rapidly to one as the number of leaves increases, at least one of these fusion gates succeeds, fusing the two clusters:



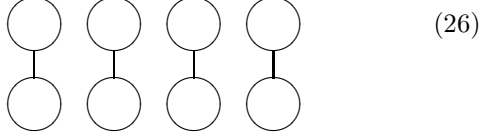
When more than one fusion gate succeeds, we can obtain the same fused cluster, simply by measuring redundant fused nodes in the computational basis². We call this process of using leaves to fuse the two clusters with high probability *parallel fusion*.

We try to create microclusters in a way that meets two complementary aims: (1) we wish to create them rapidly, in order to minimize the effects of noise; and (2) we wish to use the fewest physical resources possible in creating the microclusters. Our microcluster creation protocol is designed with both these goals in mind; somewhat better

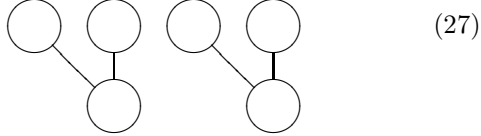
² In fact, the operations we need to do can even be accomplished without removing any redundant nodes, and this is the approach we take in our simulations. In particular, imagine that k of the simultaneous fusions succeed, resulting in k qubits in a position where there should be just one. It can be shown that this cluster state is stabilized by (that is, is a +1 eigenstate of) a tensor product of X s on any even number of those k qubits. This shows that if we were to later measure one of the k qubits in the X basis, as part of the normal running of the cluster, then the state of each of the other $k - 1$ extra qubits would collapse to an eigenstate of X , thus automatically disentangling them from the cluster without the need for further measurements. Note that there is a potential advantage in measuring the extra qubits anyway, in the X basis, to verify the measurement outcome of the first qubit. However, we do not perform this type of verification in the simulations.

thresholds could be obtained at the expense of using more resources.

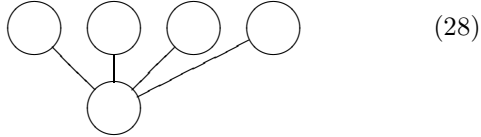
When the number of leaves is a power of two, e.g., $k = 2^m$, we create the microcluster as follows. We begin with 2^m one-leaf microclusters, which are just Bell pairs:



We then fuse pairs of the one-leaf microclusters in order to create two-leaf microclusters:



We continue in this way, repeatedly fusing the root nodes of pairs of microclusters, obtaining microclusters with ever more leaves. For the 4-leaf case, the process terminates at the next stage:



The protocol when the number of leaves is not a power of two is a straightforward modification.

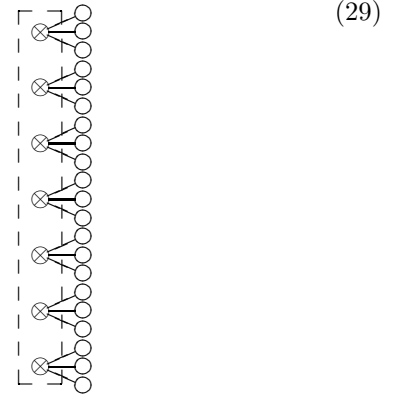
When preparing the microclusters, the fusion gates will inevitably sometimes fail. However, by doing a large number of attempts to create the microcluster in parallel, we can ensure that with very high probability at least one of these attempts will be successful. For simplicity, in our simulations we assume that fusion gates are *always* successful during microcluster creation (but not in general). This is justified because the experimenter can always postselect during microcluster creation. With this postselection, the expected number of Bell pairs consumed per k -leaf microcluster is k^2 , and it takes $\log_2(k) + 1$ time-steps to create the microcluster.

Our use of postselection in microcluster creation is merely one place at which we use postselection. It can be used whenever performing manipulations on clusters that do not contain any of the data being processed. This will include ancilla and telecorrector creation, which actually contain the bulk of the operations performed in our computation. This is extremely convenient, for it enables us to assume that non-deterministic operations have been performed successfully, at the expense of requiring the experimenter to perform a number of attempts at such operations in parallel, and to postselect on the successful operations. It will be important for us to keep track of the scaling involved in such postselection, to ensure that no exponential overheads are incurred.

2. Input states

The trials we simulate consist of multiple rounds of clusterized quantum error-correction. To describe how these rounds occur we must first specify the form of the state which is input to a round. The first round of error-correction is, of course, somewhat special, since it's the initial state of the entire computation. Nonetheless, it has the same general form as the inputs to any other round. Therefore, we begin by describing the general case, before discussing some caveats specific to the initial state of the entire trial.

The state of our optical cluster-state computer at the start of any given round is of the following form:



This is not (quite) a cluster state. To describe the state in the ideal case, consider the following two-stage preparation procedure³: (1) prepare the boxed qubits (i.e. the root nodes) in the encoded state of the corresponding qubit; and (2) attach bonds to the leaves according to the standard definition. We will make use of the leaves in the manner described earlier, to enhance the probability of fusing this input cluster to the telecorrector state (described later), which is used to effect the error-correction. As pictured, we have three leaves per root node, however in simulations this number may be varied.

Of course, in practice, the actual state will be related to this ideal state by a Pauli frame, and possibly also affected by noise in the Pauli frame, and on the physical qubits. These deviations are described using the techniques we have already introduced. Furthermore, in practice the root nodes will typically have been premeasured, and so won't actually be physically present. However, as we have argued earlier, it is often convenient to carry out the analysis as though operations were done in a different order than is actually the case physically, and so we will sometimes describe the computation as though the root nodes (and the associated local Pauli frames) are present at the beginning of the round.

³ This is, of course, not the actual procedure used to obtain the state, but merely a convenient way of describing what the state is.

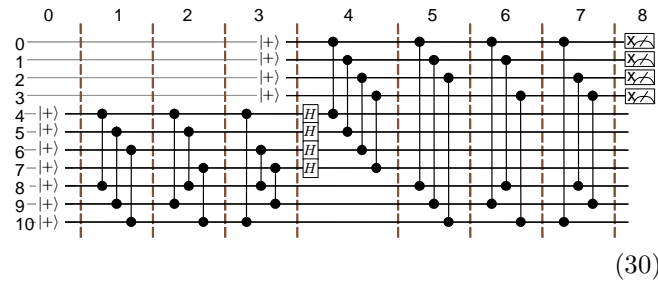
At the beginning of the entire trial, we assume the input is a noise-free state of the form depicted in Equation (29). Of course, in practice, the actual state at the beginning of the computation will be noisy. However, this noise-free assumption is justified on the grounds that the initial state does not actually matter, since our goal is to estimate the rate *per round* at which crashes are introduced into the encoded data. Following Steane [24], we perform some number of “warm-up” rounds of error-correction before beginning to gather data on this crash rate, in order to avoid transient effects due to the particular choice of initial state. The reason for starting with a noise free state is because it is a reasonable approximation to the actual (noisy) state of the computer after many rounds, and thus the transient effects can be expected to die out relatively quickly compared with many other possible starting states.

3. Ancilla creation

Each round of quantum error-correction involves the creation of some number of verified ancilla states, which are used to extract syndrome bits. These states are analogous to the ancillas used in standard fault-tolerant quantum computation. The exact number of ancillas required may vary from round to round; we describe later the details of how they are integrated into the computation.

In this section we describe the cluster-state computation used to prepare a single ancilla. This computation is essentially a clusterized version of Steane’s [41] ancilla creation circuit. We will describe this for the case of the Steane 7-qubit code, but the procedure generalizes in a straightforward manner to many other Calderbank Shor Steane (CSS) codes, including the 23-qubit Golay code used in some of our simulations⁴.

Following Steane, we can create an ancilla for the 7-qubit code using a quantum circuit of the form:

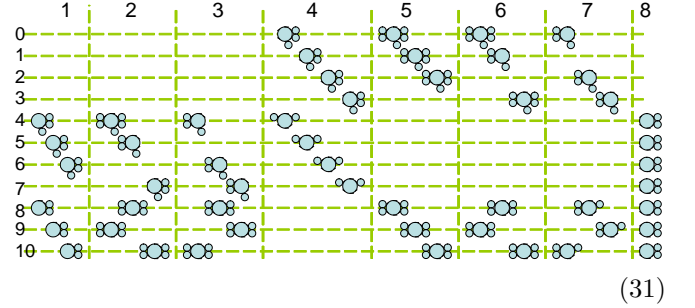


We clusterize this following the standard procedures (as described in Section II A) for clusterization, but optimized in order to meet two complementary goals: (1)

⁴ The 23-qubit Golay code is derived from the classical binary Golay code, whose defining parity check matrix is given in, for example, Sec. 5.3.3 of [42] and online at [43].

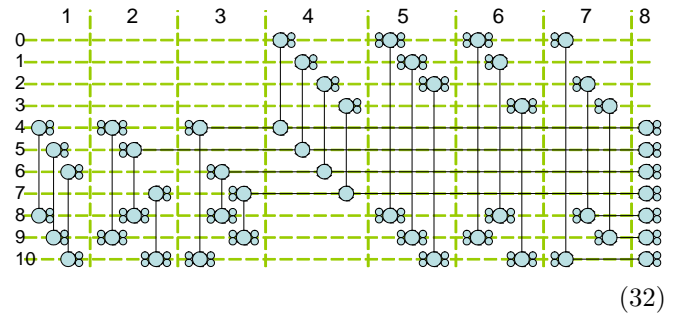
we do many operations in parallel, in order to reduce the effects of noise; and (2) careful use of postselection, in order to prevent a blow out in resource usage.

We begin the clusterization by creating an array of microclusters:



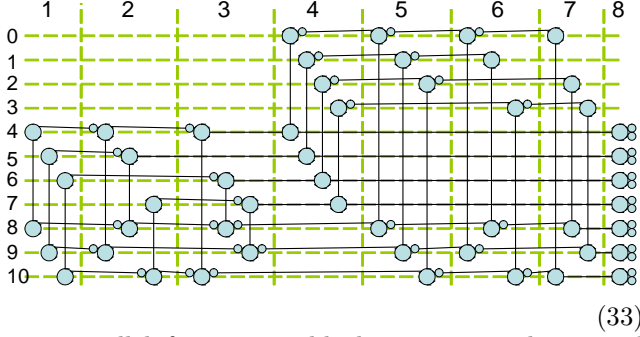
For clarity we have abridged our microcluster notation, omitting the bonds, and just drawing the nodes; the large circles are root nodes, while the small circles are leaf nodes. The co-ordinates in our microcluster array (denoted by the dashed lines and numbered labels) correspond directly to the co-ordinates in the Steane circuit. The only exception is the final column of the microcluster array, which corresponds to the output of the cluster-state computation. Nontrivial gates in the Steane circuit are replaced by microclusters, while memory steps do not require additional microclusters, and so we omit these where possible.

Our next goal is to create the following bonded microcluster array:



We do this in two steps. The first step is to attempt creation of all the *vertical* bonds, by fusion of appropriate leaves and roots. By postselection we can assume that all of these fusions were successful and no photon loss was detected. In reality, the experimenter will need to create a larger array of microclusters, and attempt all the fusions simultaneously, discarding wherever unsuccessful. The second step is to create the horizontal bonds, again by fusions of the appropriate leaves and roots, and using postselection to ensure success.

The final step is to obtain the cluster:



using parallel fusion to add the remaining horizontal bonds. The reason we use parallel fusion at this stage is to reduce the cost of postselection. The horizontal bonds added at this stage connect large parts of the cluster, and so a failure of any will result in the need to start over, and thus it is important to ensure a high probability of success, in order to reduce resource usage.

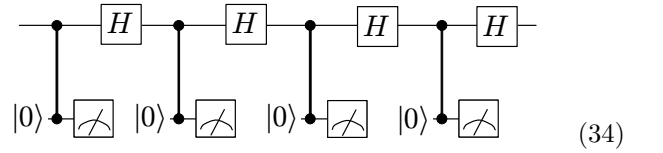
Note that, as illustrated, parallel fusion involves 2 attempted connections. However, the number of attempted connections is a variable of our simulation, and in practice we have been using 3. Varying this figure will affect both the noise threshold and the resource usage. A value of 1 is the best choice with respect to the noise threshold, since the microclusters used would be smallest in this instance, thus creating less opportunities for noise to be introduced. The corresponding resource overhead would be particularly bad though, due to the very small probability ($\frac{1}{2^{29}} \approx 2 \times 10^{-9}$ for the 7-qubit code) of fusion gates in the final step of ancilla cluster creation all succeeding. Using 3 attempts per parallel fusion, the probability of success of the final step increases to $\frac{7^{29}}{8^{29}} \approx 0.02$. If the number of attempts per parallel fusion is made too large, the benefit to the resource usage due to the higher probability of success is outweighed by the expense of creating large microclusters at the beginning. We have not performed a detailed analysis of the optimal choice for this parameter, rather we have chosen 3 as a reasonable trade-off between noise performance and resource usage.

To conclude the ancilla preparation, we simultaneously measure all remaining qubits in the X basis, except those qubits in column 8, applying the standard rules for Pauli frame propagation. To verify the ancilla, we postselect on the measurement results of the terminating qubits in rows 0, 1, 2, 3 all being 0. The resulting state is identical to the state illustrated in another context in Equation (29), with the encoded state being a $|+\rangle$. By contrast, the output of Steane's circuit-based procedure is an encoded $|0\rangle$. The difference between our protocol and Steane's is due to the presence of the extra horizontal bond between columns 7 and 8, which effects an encoded Hadamard operation. This will be compensated by a subsequent encoded Hadamard operation, described below.

4. Telecorrector creation

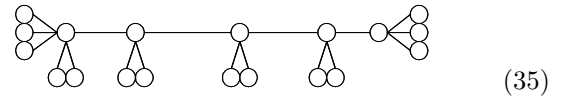
To perform error correction we need to interact the data in our cluster-state computer with the ancilla states in order to extract the error syndrome. We do this using a special cluster state which we call a *telecorrector*, which incorporates both multiple ancilla states, as well as the cluster-based machinery to effect the necessary interactions. The telecorrector arises by clusterizing Steane's protocol, but, as we shall describe, the cluster protocol enables several modifications to improve the quality of the syndrome extraction. As in the previous section, our description is adapted to the Steane 7-qubit code, but is easily modified for many other CSS codes.

Our clusterized method of syndrome extraction is based on the following quantum circuit for syndrome extraction



where operations are being performed on encoded qubits, $|0\rangle$ is fault-tolerant ancilla creation, and the measurement is a transversal X basis measurement on constituent physical qubits in the code. Circuit (34) is analogous to Steane's circuit, except that the number of syndrome extractions is fixed, and the syndrome extractions are performed in a different order: X, Z, X, Z , in contrast to Steane, who extracts all X information first, followed by all Z . The reasons for these differences are explained below.

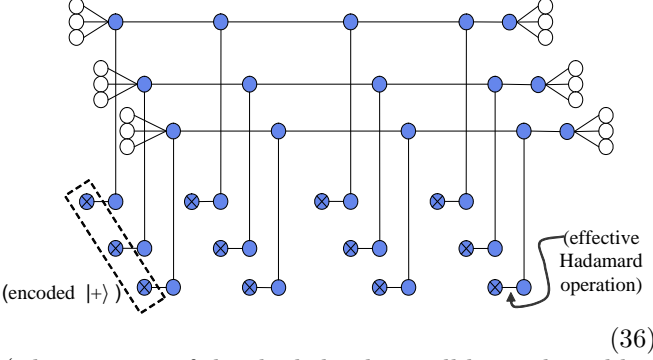
Telecorrector creation begins with the creation of 7 copies of the following state:



This state can be created in the obvious way using post-selected microcluster fusion. The leaves on the left-hand end will eventually be used to attach to a single qubit of the encoded data using parallel fusion. The leaves and root node on the right-hand end will contain the output of this round of error-correction, and become the input to the next round of error-correction. The remaining leaves will be used to fuse to ancilla states.

Simultaneous with the creation of Cluster (35), we create four verified ancilla states, using the technique described in Section VC3. We then fuse the ancillas with

the leaves on Cluster (35) to create the state:



(The meaning of the shaded qubits will be explained below). Note that we have illustrated this as though only three qubits are involved in the code: the case of 7 (or more) qubit codes is similar, but the diagram would be larger and more cluttered.

The next step is to measure all the shaded qubits in Cluster (36) in the X basis, leaving only the left-most and right-most leaves, for later use in attaching the data, and future rounds of error-correction.

Applying the propagation rules for the Pauli frame, it can be shown that the pattern of measurement outcomes from the shaded qubits completely determines whether or not the repeated syndrome measurements will agree.

This is a remarkable property, since it enables us to determine whether the repeated syndrome measurements will agree *before* the state has even interacted with the data. Furthermore, we can take advantage of this by postselecting on obtaining a set of measurement outcomes that ensure this *preagreeing syndrome* property. We call the postselected state with this preagreeing syndrome property the *telecorrector*.

Once prepared, we use parallel fusion to attach the telecorrector to the data, and then X basis measurements to complete this part of the cluster-state computation. Standard propagation rules are used to update the Pauli frame, and to determine the final syndrome extracted from this procedure. We describe in the next section how this syndrome information is decoded in order to perform correction.

The preagreeing syndrome property is responsible for the different number and order of syndrome extractions in our protocol as compared with Steane's. Steane needs to extract many syndromes (more as the code gets larger) in order to make it likely that some large subset of those syndromes agree. In any round where syndromes don't agree, correction cannot take place, and the round just adds more noise to the data. We avoid this issue by using the preagreeing syndrome property, thus reducing the number of locations at which noise can be introduced into the data.

The preagreeing syndrome property also accounts for the order in which we extract syndromes. In Steane's protocol, the order of syndrome extractions is all X extractions in succession followed by all Z extractions, so as to maximize the chance of obtaining syndromes that

agree. By extracting syndromes in the order X, Z, X, Z we reduce the chance of agreeing syndromes (for a small cost in resource usage) but gain the ability to detect and postselect against additional types of noise. In particular, X errors that propagate from the second ancilla to become X errors on the data will be detectable via a disagreement of the first and third syndromes. Likewise, X errors that propagate from the third ancilla to become Z errors on the data will cause the second and fourth syndromes to disagree.

5. Reduction of fusion gate failure and photon loss to Pauli errors

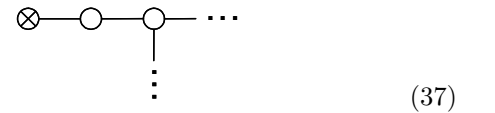
During the preparation of the ancilla and telecorrector states we used postselection to avoid dealing with fusion gate failure and photon loss. This has the advantage both of improving the threshold, and also means that our simulations don't need to describe these errors. However, when the telecorrector is joined to the data, it is no longer possible to postselect against these types of error, and we must find some way of modeling them in our simulations.

By following a suitable experimental protocol, it turns out that both these types of errors can be reduced to a (located) Pauli-type error, which we already know how to model in our simulations. The purpose of this section is to describe this reduction.

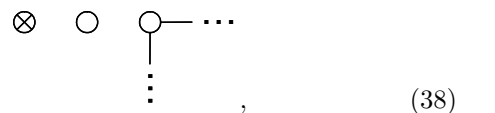
In practice, we believe the protocol for reduction we describe is likely to slightly worsen the behaviour of the cluster-state computation. The reason for introducing the reduction is therefore not to improve the threshold, but rather to simplify our simulations, and the statistics that we gather. In actual experiments, the special steps in the protocol described in this section would not need to be performed, and the threshold would be slightly higher than our simulations indicate.

We begin with a description of how we treat fusion gate failure. The discussion of photon loss will follow similar lines.

Suppose we are attempting to connect the telecorrector to the data using parallel fusion, and all attempts fail, for a particular horizontal row of qubits. The result of such a failure will be missing horizontal bonds in the cluster. That is, instead of obtaining the desired cluster



we obtain



where the crossed node indicates a root node of the input data. We can think of this as two located (i.e., known by

the experimenter) CPHASE errors. (Note that in reality, the central bare node in Equation (38) is not present, due to the destructive measurement occurring with fusion failure. For the sake of the present argument, we shall imagine that the experimenter has brought in a new $|+\rangle$ state in this instance.) Unfortunately, our error model for simulations doesn't allow us to describe CPHASE errors directly. Although we could imagine adding such an error to our list of possible error types, the propagation rules turn out to be rather complex, and we wish to avoid this if possible.

Suppose, however, that when parallel fusion fails, the experimenter does the following:

- Depolarizes all three nodes of Equation (38) (that is, replaces the state of the three qubits by the maximally mixed state).
- Notes the location of the row in which the failure occurred, for use in decoding.
- Carries out the rules for propagating the Pauli frame, as though the fusion gate had succeeded, and the horizontal bonds created.

Once the experimenter has performed the depolarization, it does not make any physical difference whether the CPHASE errors occurred or not, and so we can imagine they have not occurred. The only remaining errors are Pauli-type errors, and so can be simulated in the standard way.

Note that the effect of the intentional depolarization as described is to randomize the results of later measurements performed on the three qubits. Thus, our reduction of fusion failures to Pauli errors could be equivalently achieved by the experimenter randomizing the measurement results, without actually performing the depolarization. Or simpler still, as a consequence of the propagation rules for the Pauli frame, the randomization of the three measurement results could be replaced by a randomization of the Pauli frame of the left-hand root node. Thus, in our simulation, when a failed parallel fusion between the data and telecorrector occurs, we simply randomize the description of the Pauli frame error of the left-hand root node. This completes the description of our procedure for modeling parallel fusion failure when attaching the telecorrector to the data.

Consider now the case of photon loss. Suppose a photon loss is detected after fusion of the data and the telecorrector. Recall from Section III that photon loss may occur in a number of physically distinct ways: immediately after Bell pair creation, before a memory step, before a fusion gate, and between the fusion gate and measurement. The effect of the photon loss may depend on which of these possible ways it arose during the computation. In particular, the effect may be described in the various cases as either CPHASE errors as in the case of failed fusion, or simply a successfully created cluster followed by a single photon-loss error. The experimenter would not know which of these cases had occurred.

To cope with this, we modify the protocol so that the effects (in any of these cases) can be simulated by a Pauli-type error. In the modified protocol the experimenter does the following after detecting a photon loss immediately after the data and telecorrector have been fused.

- If a missing photon has been detected, the experimenter randomizes the local Pauli frame of the corresponding data qubit, i.e., the left-hand root node.
- Notes the location at which the photon loss occurred, for use in decoding.
- Carries out the rules for propagating the Pauli frame as though the horizontal bond between data and telecorrector had been successfully created.

This is simulated in the obvious way: when a photon loss is detected after fusion of data and telecorrector, we randomize the Pauli frame error of the corresponding data qubit, and apply the standard propagation rules⁵. The justification for following this procedure is very similar to fusion gate failure, but requires the consideration of more separate cases, corresponding to the different possible points of photon loss. We omit the details.

Note that a significant advantage of the frequent measurements performed in the cluster model is that photon loss is detected before it has a chance to propagate to adversely affect other parts of the computation. This is particularly useful as postselection can be used to ensure that ancillas are free of photon loss noise, which helps improve the threshold.

6. Decoding

We use a non-standard technique for syndrome decoding, designed to take advantage of the knowledge the experimenter has of the locations of errors caused by photon loss and nondeterminism. Our technique is a maximum likelihood procedure for decoding arbitrary combinations of located and unlocated errors.

We take advantage of the fact (see, e.g., Exercise 10.45 on page 467 of [17]) that a code able to correct t unlocated errors is also able to correct $2t$ located errors. This is particularly advantageous for optical cluster-state computation, since parallel fusion failure and photon loss errors are likely the dominant types of noise.

Both the codes we will use in simulations (Steane 7-qubit and Golay 23-qubit) are CSS codes with the property that decoding of the X and Z errors can be performed separately using an identical procedure. Our description will be for the case of X decoding; the Z follows similar lines.

⁵ One slight simplification we make in our simulations is to assume that photon loss may occur even following *failed* fusion gates. This can only worsen the thresholds obtained from our simulations, but the effect is negligible.

The decoding routine has the following inputs: the measured X -error syndrome, obtained by applying the classical parity check matrix to the vector of total errors of the ancilla measurement outcomes; and a list of locations (qubit indices within the code block) at which located errors have occurred during the round. The outputs to the decoding routine are: a list of locations where X flips should be made in order to correct the data; and a flag signaling a *located crash*.

The located crash flag indicates that the correction has likely failed, and the logical state of the data has effectively experienced a random X operation (i.e. an X *crash*). This situation arises when two different patterns of X errors are found to have equal maximum likelihood, but differ from each other by a logical X operation. The located crash flag is not used directly, but will be used to assist decoding at the next level of concatenation, by identifying encoded blocks which are known to have experienced an error. By feeding information in this way to higher levels of concatenation, we are increasing the overall noise-threshold performance of the protocol.

Before describing our maximum likelihood decoder, we first give a simple model for the relative likelihood of errors. The total X error pattern on the data is a product of X s due to unlocated errors, and X s due to located errors. The measured syndrome is assumed to be the bitwise exclusive or of the syndromes of the two error patterns. The likelihood of a pattern of unlocated X s is assumed to be a decreasing function of weight, but not a function of how the errors are positioned. The likelihood of a pattern of X errors due to located errors is uniform across all patterns which have I wherever located errors have not occurred. This is due to our reduction of located errors to depolarization. For example, if located errors have occurred on three qubits, then the resulting X error pattern on those qubits due to the located errors will be either III , IIX , \dots , XXX with equal probability, and I on other qubits.

To decode, we loop over all possible values for the located error pattern, and for each one we determine the most likely unlocated error pattern. For a particular located error pattern, the most likely unlocated error pattern is found by first finding its syndrome, by taking the exclusive or of the measured syndrome with the syndrome of the located error pattern. Then from this syndrome, the most likely unlocated error pattern is found via a standard decoding array. As the loop is repeated over all located error patterns, we keep track of which “most likely unlocated error pattern” has the overall minimum weight, and is thus most likely overall. If this minimum is unique, then the data is corrected⁶ by first correcting

for this minimum weight unlocated error pattern, then correcting for the corresponding located error pattern. The located crash flag is set to “false”.

Otherwise, if the minimum is not unique, we arbitrarily choose one of the minimum weight patterns and corresponding located error pattern, and correct accordingly. We compare the correction performed against the corrections associated with each of the other minima. If they are all equivalent up to stabilizer operations of the code, then we set the located crash flag to “false”. Otherwise we set the located crash flag to “true”.

7. Results of the optical cluster simulation

To determine the threshold for a concatenated error correction protocol, we must analyse how the effective error rates vary as more levels of concatenation are added. We now give results of this analysis for the lowest level of concatenation – the cluster-based protocol of Subsection VC. We simulated this protocol with the aim of categorizing the function that maps the physical noise parameters (ϵ, γ) to the logical error rates, or *crash* rates, defined below. Likewise, in subsection VD we describe simulations which categorize the similar function for a deterministic circuit-based protocol, representing higher levels of concatenation. In subsection VE, the results are combined to give the threshold region for concatenated cluster-state optical quantum computing.

Two of the authors, CMD and HLH, each created a version of the simulator, and no program code was shared between the two versions. This duplication was done so that agreement between the results of the two simulators could act as a verification that the simulators were bug free. The programming languages C++ and C were used for the most part (and to a lesser extent, Python and MATLAB).

At the end of a round of simulated cluster-based error correction, we say that the round has caused a *located crash* whenever either the X or Z decoding steps in that round has reported a located crash. Note that the imagined experimenter would be aware of located crashes occurring. In addition, we define an *unlocated crash* as follows. We take the pattern of total Pauli errors on the root nodes of the data, and consider the result of a perfect (noise-free) round of correction. If perfect correction would result in a pattern of Pauli errors equivalent to an encoded X , Y , or Z Pauli operation, then we say the data has experienced an unlocated crash. Note that errors on the leaves of the data are not taken into account when we test for an unlocated crash. Such errors are not completely ignored, as they will instead propagate to the next round of error correction and affect the next crash rate test.

⁶ Note that in both the cluster-based and deterministic protocols we don’t ever physically apply the corrections. Instead, by “correcting” the data we simply mean that we keep track of the corrections that must be applied, and propagate them forward through the computation to be compensated at the end, much

as we treat the Pauli frame.

We performed four separate sets of simulations, in order to compare the use of two different codes and two different settings for memory noise. The four configurations were: Steane 7-qubit code with and without memory noise enabled; and the Golay 23-qubit code with and without memory noise enabled. In the cases where memory noise was disabled, we did not apply photon loss or depolarization noise during memory operations. Comparing the results with memory noise enabled and disabled gives an indication of how significant the effect of memory noise is on the performance of the protocol.

For each of the four configurations noted above, we chose a number of settings for the noise parameters (ϵ, γ) , and for each we ran a many-trial Monte Carlo simulation. Each trial of the Monte Carlo simulation consisted of two successive rounds of the error correction protocol, and the outcome of the trial was determined by whether the second of the two rounds caused a crash. The purpose of the first “warm-up” round is to reduce the transient effects due to our choice of (noise free) initial conditions. We found that including more than one warm-up round did not make a statistically significant change to the results. However, not including a warm-up round did affect results considerably.

The number of parallel attempts per leaf-to-leaf fusion during ancilla cluster creation and during the joining of ancilla to the telecorrector was set to 3 throughout. Recall, as far as the noise performance is concerned, the fewer attempts per leaf-to-leaf fusion the better during the above mentioned cluster building steps. However we chose 3 as a compromise between noise performance and resource usage.

The number of parallel attempts per leaf-to-leaf fusion when joining a telecorrector to the data cluster was set at five throughout. Here, fewer attempts is not necessarily better for noise performance, because when all attempts fail, a located error is introduced to the data. We found that using any figure above five gave a consistently worse final threshold, whereas a figure less than five gave a worse threshold for small values of γ but a slightly better threshold for larger γ values.

The various outcomes of each trial are tallied as follows. For all the trials for which the first round does not cause a crash, we count: (1) the number N_U of trials for which the second round causes an unlocated crash but not a located crash, (2) the number N_L of trials for which the second round causes a located crash, and (3) the number N_N of trials for which no crashes occur.

From the values N_U , N_L , and N_N , the unlocated and located crash rates E and Γ are estimated as follows:

$$E = \frac{N_U}{N_U + N_N}, \quad (39)$$

$$\Gamma = \frac{N_L}{N_U + N_N + N_L}. \quad (40)$$

Note that we omit N_L from the denominator of E since we only compute the unlocated crash rate conditional on

no located crash having occurred. The estimated standard error for E and Γ respectively are

$$\sigma_E = \frac{\sqrt{N_U}}{N_U + N_N}, \quad (41)$$

$$\sigma_\Gamma = \frac{\sqrt{N_L}}{N_U + N_N + N_L}. \quad (42)$$

Both these expressions arise from the fact that if we sample N times to estimate the probability p of an event occurring, then the standard deviation in the estimate is $\sqrt{p(1-p)/N}$. When p is small, as it is in our case, we may neglect the $1-p$ term to obtain a standard deviation of $\sqrt{p/N}$.

The two versions of the simulator program code were compared as follows. For 65 different settings of (ϵ, γ) , the values (E, Γ) were estimated from each simulator using a sample size of at least 10^6 . This was done for the 7-qubit code, both for memory noise disabled and enabled. For the resulting 130 different values, we compared the results obtained by the two simulators, and the largest difference observed was 3.1 times the estimated standard error. In other words, the two independently-created simulators showed excellent agreement, and this provides additional evidence that they are free of serious bugs.

One of the versions of the simulator code was used to gather final results. We denote the particular choices of the input noise parameters as (ϵ_i, γ_i) , $i = 1, \dots, D$, the corresponding crash rate estimates as E_i and Γ_i , and the corresponding standard errors as σ_i^E and σ_i^Γ . For the 7-qubit code, approximately 10^7 samples were run for each of 59 different settings of the noise parameters (ϵ_i, γ_i) , for both disabled and enabled memory noise. (Note that the particular choices used for (ϵ_i, γ_i) are shown as small circles on the threshold plots in the final results subsection, V E).

For the 23-qubit code, samples were gathered for 43 different noise parameter settings, for both enabled and disabled memory noise. The sample sizes ranged from 4×10^4 to 3×10^7 for disabled memory noise, and from 3×10^5 to 2×10^7 for enabled memory noise. The smaller sample sizes correspond to highest noise rate settings, where the simulation becomes much slower (due to noisy ancilla and telecorrectors being discarded more often, an effect which is much more pronounced for the 23-qubit code compared with the 7-qubit code).

We fit polynomials to the data using weighted least-squares fitting. A polynomial $E(\epsilon, \gamma)$ is fitted to the values E_i by minimizing the following residual:

$$R_E = \sum_{i=1}^D \frac{(E(\epsilon_i, \gamma_i) - E_i)^2}{(\sigma_i^E)^2}. \quad (43)$$

Likewise, the polynomial $\Gamma(\epsilon, \gamma)$ is fitted to the values Γ_i by minimizing the residual:

$$R_\Gamma = \sum_{i=1}^D \frac{(\Gamma(\epsilon_i, \gamma_i) - \Gamma_i)^2}{(\sigma_i^\Gamma)^2}. \quad (44)$$

Monomial	Coefficient
ϵ	0.003357
$\epsilon\gamma$	2209
$\epsilon\gamma^2$	-3.630×10^6
$\epsilon\gamma^3$	1.868×10^9
$\epsilon\gamma^4$	-8.421×10^{10}
ϵ^2	2009
$\epsilon^2\gamma$	-2.133×10^7
$\epsilon^2\gamma^2$	2.979×10^{10}
$\epsilon^2\gamma^3$	-2.573×10^{12}
ϵ^3	-3.578×10^7
$\epsilon^3\gamma$	2.348×10^{11}
$\epsilon^3\gamma^2$	-2.9574×10^{13}
ϵ^4	7.098×10^{11}
$\epsilon^4\gamma$	-2.341×10^{14}
ϵ^5	-2.472×10^{14}

TABLE I: The polynomial $E(\epsilon, \gamma)$ as fitted to the unlocated crash rate data, for the cluster-state protocol, using the 23-qubit code with memory noise enabled.

All terms up to order five were included in the polynomial $E(\epsilon, \gamma)$, with the exception of terms of order 0 in ϵ . The reason for the excluded terms is that we know $E(0, \gamma) = 0$. In the polynomial $\Gamma(\epsilon, \gamma)$, all terms up to order six were included for the 23-qubit code results, and terms up to order five were included for the 7-qubit code. In each case the chosen orders of five or six were the minimum that gave a “good” fit to the data for all four configurations of code and memory noise. We considered a good fit to be when the residual divided by the number of data points D was roughly of order 1 (in practice the value ranged from 0.42 to 1.43 for the eight polynomials fitted). Such a condition indicates that the differences between the observed values and the fitted polynomial could reasonably be accounted for solely by the errors due to the finite sample size.

It would be rather cumbersome to give all the fitted polynomials obtained, in isolation from the procedure in Subsection V E to convert this information to a threshold region. Rather, as an example of the results, we give the coefficients of the polynomial $E(\epsilon, \gamma)$ for the case of the 23-qubit Golay code with memory noise enabled, in Table I.

D. The deterministic protocol

In this subsection we describe the simulation of our deterministic (circuit based) error-correction protocol. Much of the detail of the protocol is given in Appendix A. The main purpose of the present subsection is to explain how the deterministic protocol fits together with the cluster-based protocol, describe the effective noise model used for simulating the deterministic protocol, and to give the methods and results of these simulations.

1. Concatenation of protocols

To perform a threshold analysis, one usually imagines that a fault-tolerant error-correction protocol is concatenated with itself many times. That is, the encoded qubits corrected by the circuit at the lowest level of concatenation are themselves used to build up a circuit for error correction at a higher level of encoding, and so on. Then, by definition, a physical error rate is “below the threshold” if the rate of logical errors (crashes) at the highest level of encoding can be reduced arbitrarily close to zero by using sufficiently many levels of concatenation. Usually, to simplify analysis, the error correction circuit and noise model at every level are taken to be identical, and the rate of noise per gate at one level is taken to be the rate of crashes per error-correction round at the next lowest level. With these set of assumptions, the task of determining if a particular noise rate is below the threshold becomes that of simulating just the lowest level of concatenation, and testing whether the crash rate is below the physical noise rate.

In the quantum computation that we are simulating, only the lowest level of concatenation uses the cluster based protocol described in subsection V C. For the second and higher levels of concatenation, we can effectively regard it as though a circuit-based deterministic protocol is being used, since the encoded gates available to higher levels of concatenation are deterministic. Steane’s fault-tolerant protocol would be a suitable choice for the higher levels of concatenation, but rather we have chosen to use the telecorrection protocol of Appendix A for the reasons we outline in that appendix.

To motivate the ensuing description of the effective noise model used in the simulations of the deterministic protocol, we discuss the way in which a gate or other operation at one level of concatenation is built from the error-correction protocol at the next lower level of concatenation. The operations used in the telecorrector circuit are: CPHASE and CNOT gates; preparation of $|0\rangle$ and $|+\rangle$; X -basis measurements; and memory. First we discuss how these operations in the level $L \geq 3$ of concatenation are built from level $L - 1$.

The memory operation at level L is simply one round of error correction at level $L - 1$. Accordingly, in our noise model for memory operations at level L , the various noise types are introduced with probabilities given by the crash rates of a round of level $L - 1$ error correction (the details will be made clear later).

Each of the two types of gates used in the telecorrection circuit at level L are implemented by first applying a round of error correction to the inputs of the gate, then applying the encoded gate consisting of the level $(L - 1)$ gate applied transversally to each qubit in the code. The error correction stage contains many more gates than the actual encoded gate, thus we assume that the majority of the noise introduced by a gate is due to the error correction step. Accordingly, in our noise model for gates at level L , noise is introduced to each of the gate inputs

according to the model for memory noise (that is, again given by the crash rates of a level $L - 1$ correction round).

The preparation of $|0\rangle$ or $|+\rangle$ at level L can be implemented by preparing the level $L - 1$ state transversally on each qubit in the code, followed by a round of error correction. Again, we assume that most of the noise is due to the error-correction step, and at level L our model introduces noise after preparation operations according to the model for a step of memory noise.

An X -basis measurement at level L is implemented by measuring each level $L - 1$ qubit transversally in the X basis, then performing classical error correction on the results. So in contrast to the other operations, measurement does not involve a quantum error correction round at the lower level, but rather a noise free classical correction. Accordingly, our noise model assigns a much lower rate of noise to measurements at level L relative to the rates of the other operations.

Similar arguments can be made for operations at level 2 built from the cluster protocol of the lowest level. Thus, we will take the rates of noise introduced to gates, memory and preparation at level 2 equal to the crash rates due to a round of clusterized error correction, but make the noise due to measurement significantly less.

We now specifically state the effective noise model used at a level $L \geq 2$ of concatenation, following the arguments above.

2. Effective noise model

In the simulation of the level $L \geq 2$ error correction circuit, we model the encoded qubits that this circuit acts upon as though they were physical qubits. That is, at every stage of the simulation of the circuit, the error description is a Pauli error, I , X , Y or Z , associated with each of the qubits. The details of the errors on lower level qubits are not directly simulated. As in the cluster-based protocol, the circuit is divided into time-steps. Each qubit in the level- L circuit can undergo one operation per time-step. The length of a time-step corresponds to the time taken for a complete round of error correction and an encoded operation to be performed at level $L - 1$.

Our model involves four types of noise, unlocated X and Z Pauli errors, and located X and Z Pauli errors. Unlocated and located errors are designed to represent the unlocated and located crashes occurring at level $L - 1$. When a qubit experiences an unlocated X Pauli error, it undergoes an X operation, unknown to the experimenter, and similarly for unlocated Z Pauli errors. When a qubit experiences a located X error, it undergoes an X operation with probability $1/2$. The experimenter will know that a located X error has occurred, but not whether the corresponding X Pauli error has actually been applied. Z located errors are similar.

When we say that unlocated noise is applied with a probability p , we mean that both unlocated X and Z

Pauli errors are applied with equal probability, and independently, such that the total probability that an error was applied is p . Similarly for located noise applied with probability q . We choose this model of independent X and Z errors because of a numerical observation that the rate of Y crashes is much less than the combined rate of X and Z crashes, for both our cluster-based and deterministic protocols. Although observed X and Z crash rates are not entirely independent, we have nonetheless chosen an independent noise model, which empirically appears to provide a good approximation to the observed behaviour.

We now describe how noise is introduced by each operation. Let p and q be the rates of unlocated and located crashes respectively for an error correction round at level $L - 1$.

- **Memory and gates:** Before the gate or memory, the following noise is applied to the input qubit, or in the case of two-qubit gates is applied independently to each input. Unlocated noise is applied with probability p , and, independently, located noise is applied with probability q .
- **Preparation:** After the preparation, unlocated noise is applied with probability p , and, independently, located noise is applied with probability q .
- **Measurement:** Before the measurement, unlocated noise is applied with probability $p/10$, and, independently, located noise is applied with probability $q/10$.

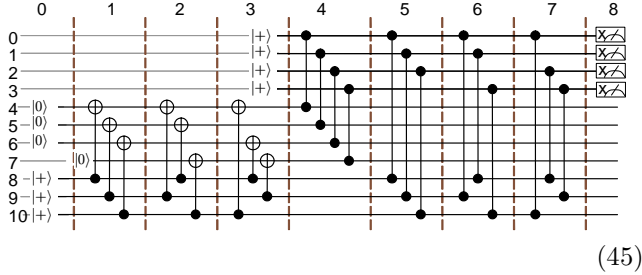
The value of one tenth for the relative strength of measurement noise is somewhat arbitrary. In reality, the relative strength of measurement noise would decrease for higher levels of concatenation, and would be generally be less than one tenth. We believe that our choice to fix the value at one tenth makes little difference to the simulation results, compared with a more accurate treatment.

3. Telecorrection protocol

We simulate the protocol described in Appendix A, in particular using the layout of Circuit (A9). We now briefly describe some further pertinent details of the protocol not given in the appendix, namely the circuit used for ancilla creation/verification, the procedure for post-selection during telecorrection creation, and the decoding procedure.

The circuit used to create and verify encoded $|0\rangle$ ancilla states, denoted by the operation “ $|0\rangle$ ” in Circuit (A9), uses the design of Steane. For example, for the seven

qubit code, the circuit is:



where the measurements are post-selected to have outcome “0”.

Note that in the case of the 23-qubit code (not shown), our circuit for ancilla creation and verification has the advantage of taking 8 fewer time steps than that used by Steane [24] for the same code. This is due to the fact that we start with a version of the classical Golay code having a reordering of the 23 bits in the code. By reordering bits in the code (i.e., permuting columns in the check matrix) and then reexpressing the check matrix in standard form, it is possible to change the maximum column and row weight of the check matrix, which has the effect of changing the number of time steps in the creation and verification circuits. After trying many random bit-reorderings, we found that the number of time steps in the circuit could be made as low as 17, compared with Steane’s 25.

The telecorrector-creation part of the protocol, indicated by the boxed region in Circuit (A9), is performed many times in parallel, and post-selected to give a successfully created telecorrector state. Here, “successful” means that syndromes of like type agree, and that no located noise occurred during the creation circuit.

During the protocol, the data and one half of the telecorrector are measured, in order to effectively apply two successive encoded transport circuits. Each of the two encoded measurements consists of X -basis measurements on each of the qubits in the code, followed by classical error correction performed on the measurement results. In each case, the correction procedure involves: (1) calculating the syndrome associated with the measurement results, (2) determining which of the individual measurement results within the encoded measurement were subject to located noise, and (3) using the results of the first two steps as input to the decoding procedure of Subsection V C 6.

4. How we simulate the protocol

A simulation trial begins with the state of the quantum computer being noise-free. Thus, the description of the initial state is a Pauli error of I on each data

qubit⁷. Then, some number of repeated telecorrection rounds are simulated. As each operation in the circuit is simulated, the Pauli error description of the qubits are updated stochastically based on the unlocated noise model, and Pauli errors are propagated as appropriate for the operation. The propagation rules for each operation are:

- Preparation: Pauli error is reset to I .
- Measurement: Measurement in the X basis causes the Z part of the Pauli error on a qubit to propagate to the measurement result, and the X part of the error to be eliminated.
- CNOT gate: A Pauli error of $X^{x_t}Z^{z_t}$ on the target and $X^{x_c}Z^{z_c}$ on the control are transformed as

$$x'_t = x_t + x_c \quad (46)$$

$$z'_t = z_t \quad (47)$$

$$x'_c = x_c \quad (48)$$

$$z'_x = z_c + z_t. \quad (49)$$

- CPHASE gate: A Pauli error of $X^{x_1}Z^{z_1}$ and $X^{x_2}Z^{z_2}$ on the two inputs are transformed as

$$x'_1 = x_1 \quad (50)$$

$$z'_1 = z_1 + x_2 \quad (51)$$

$$x'_2 = x_2 \quad (52)$$

$$z'_2 = z_2 + x_1. \quad (53)$$

To speed up simulations, located noise is not introduced where it will later be post-selected away. Located noise which cannot be post-selected away occurs due to the following operations in the protocol: the transversal CPHASE between the data and the one half of the telecorrector; the memory step on the other half of the telecorrector during the aforementioned transversal CPHASE; and the measurements of the data and one half of the telecorrector. A straightforward analysis of error locations shows that the effect of all these located noise events is statistically equivalent to applying a located error at the start of the round with a suitable probability. We omit the details of this analysis, but note that for simplicity in simulation we used this simplified error model.

5. Results of simulating the deterministic protocol

As in the simulations of the cluster-based protocol, we aim to categorize the function which maps input noise

⁷ Note that the Pauli frame, used in the optical cluster protocol, does not form part of the deterministic protocol. Thus we do not keep track of Pauli frame errors when simulating the deterministic protocol.

parameters, in this case the unlocated noise rate p and located noise rate q , to the logical error rates, being the unlocated crash rate P and located crash rate Q . From knowledge of this map for both the cluster-based and deterministic protocol, the overall threshold region can be determined.

Again we performed separate sets of simulations using the 7-qubit Steane code with and without memory noise enabled, and using the 23-qubit Golay code with and without memory noise enabled. Note that in the case where memory noise is disabled, we still apply memory noise on the bottom half of the telecorrector during the timestep in which the data and top half of the telecorrector are interacting with the CPHASE gate. This location in the circuit is where any encoded gate would be performed between correction rounds, and so we apply noise here in every circumstance so that the noise due to this encoded operation is taken into account.

For a particular choice of code and memory noise setting, we chose a number of settings for the parameters (p, q) , and for each we ran a many-trial Monte Carlo simulation. As for the cluster-state simulations, each trial of the Monte Carlo simulation consisted of two successive rounds of the error correction protocol, with statistics gathered on the rate of crashes introduced by the second round. Again, including more than two rounds did not appear to affect results.

The definition of unlocated and located crashes for a round of the deterministic protocol is virtually identical to that given in subsection VC7. Similarly, the tallies N_L , N_U and N_N for the various trial outcomes share the same definition as in subsection VC7.

The unlocated and located crash rates P and Q are estimated as follows:

$$P = \frac{N_U}{N_U + N_N}, \quad (54)$$

$$Q = \frac{N_L}{N_U + N_N + N_L}. \quad (55)$$

The estimated standard error for each quantity is

$$\sigma^P = \frac{\sqrt{N_U}}{N_U + N_N}, \quad (56)$$

$$\sigma^Q = \frac{\sqrt{N_L}}{N_U + N_N + N_L}. \quad (57)$$

The results of two independently-written simulators were compared, as in the case of the optical cluster state protocol, as a check on whether the results were bug free. Estimates of the quantities P and Q were compared between the two versions of the simulator, using the 7-qubit code and a sample size of approximately 10^6 , for 68 different noise settings with memory noise disabled and 86 different noise settings for memory noise enabled. Comparisons of a lesser sample size were also carried out for the 23-qubit code. The largest discrepancy found during all comparisons equated to 3.2 times the estimated

standard deviation. Thus the two simulators showed excellent agreement, and this provides additional evidence that they are free of serious bugs.

Final results were gathered using one of the versions of the simulator. Denote the choices of the input noise parameters as (p_i, q_i) , $i = 1, \dots, D$, the corresponding crash rate estimates as P_i and Q_i , and the corresponding standard errors as σ_i^P and σ_i^Q . Polynomials were fitted to the data using weighted least-squares fitting. A polynomial $P(p, q)$ is fitted to the values P_i by minimizing the following residual:

$$R_P = \sum_{i=1}^D \frac{(P(p_i, q_i) - P_i)^2}{(\sigma_i^P)^2}. \quad (58)$$

Likewise, the polynomial $Q(p, q)$ is fitted to the values Q_i by minimizing the residual:

$$R_Q = \sum_{i=1}^D \frac{(Q(p_i, q_i) - Q_i)^2}{(\sigma_i^Q)^2}. \quad (59)$$

All terms up to order six were included in the polynomial $P(p, q)$, with the exception of terms of order 0 in p . In $Q(p, q)$, all terms up to order five and eight respectively were included when using the 7 and 23-qubit codes, except terms of order 0 in q . The reason for the excluded terms is that we know $P(0, q) = 0$ and $Q(p, 0) = 0$. The orders were chosen using a similar criteria as for optical cluster protocol.

To present the results of the deterministic simulations, we calculate a threshold region with respect to the noise parameters at the second level of concatenation. (Thus, we are temporarily ignoring the effect of the optical cluster protocol at the lowest level). Define the map $g : (p, q) \rightarrow (P(p, q), Q(p, q))$, where P and Q are the fitted polynomials. If (p, q) are the effective unlocated and located noise rates at the second level of concatenation, then the unlocated and located crash rates at the k -th level may be estimated by computing $g^{(k-1)}(p, q)$. Provided this tends towards $(0, 0)$ as $k \rightarrow \infty$ the point (p, q) is inside the threshold region for the deterministic protocol. It is possible to test many thousands of points very quickly using this method, giving the threshold to high resolution.

The threshold regions for the simulations using the 7 qubit code are shown in Figure 2. For each of the points (p_i, q_i) shown by the circles, between 10^7 and 2×10^7 trials were run. Threshold regions for the simulations using the 23 qubit code are shown in Figure 3. The number of trials run per point (p_i, q_i) ranged from approximately 2×10^5 to 4×10^7 . For the upper plot in Figure 3 we have estimated the error in the threshold due to the finite sample size of the simulations. This rough estimate of the error was obtained by repeating the polynomial fitting a further 20 times, using the same set of data (P_i, Q_i) , but subject to additional additive Gaussian noise of standard deviation (σ_i^P, σ_i^Q) . The largest and smallest values of the threshold obtained through this process are plotted

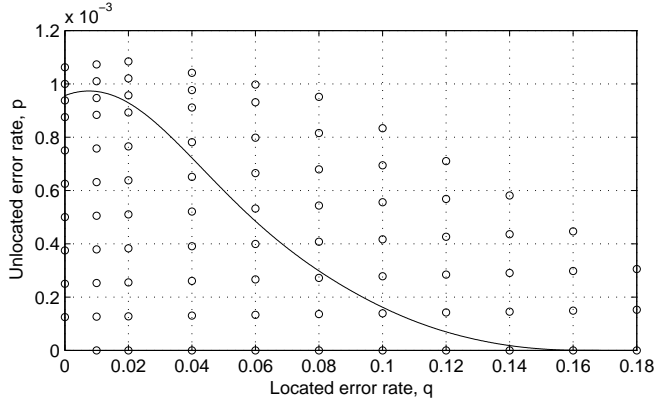
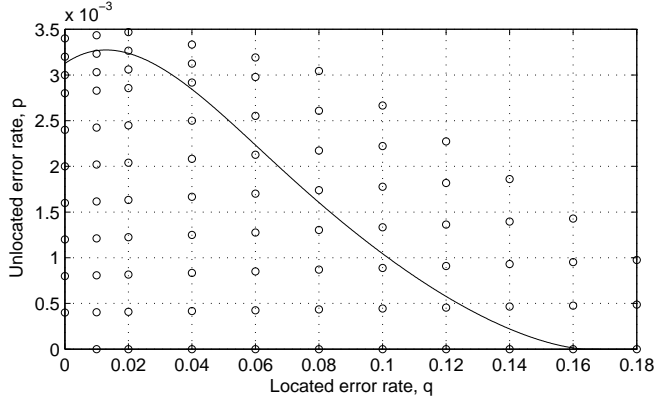


FIG. 2: Threshold region (below the solid line) for the deterministic protocol using the 7-qubit Steane code. Memory noise is disabled top, and enabled bottom. Circles indicate the noise parameter values for which the simulation was run.

as the dashed lines. The estimated error for the other three plots in Figures 2 and 3 is not shown, but is smaller in these cases.

The threshold with respect to unlocated noise can be compared to circuit-model thresholds obtained by other authors (keeping in mind though that noise models and resource usage vary substantially between different authors). Our best threshold for unlocated noise for the four plots in Figures 2 and 3 is approximately 8×10^{-3} , for the 23-qubit code with no memory noise. This compares with a threshold of 3×10^{-3} obtained by Steane [24], 9×10^{-3} by Reichardt [44], and 3×10^{-2} by Knill [23].

A feature of our threshold plots worth noting is the dramatically larger threshold for located noise (up to 0.25 for the Golay code) as compared to that of unlocated noise. Thus, the use of post-selection in the protocol combined with a purpose-built decoding routine has had a dramatic positive effect on the threshold for unlocated noise.

Note also that all threshold regions in Figures 2 and 3

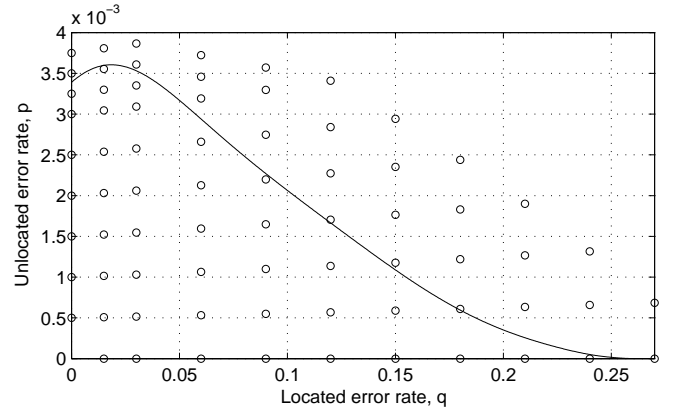
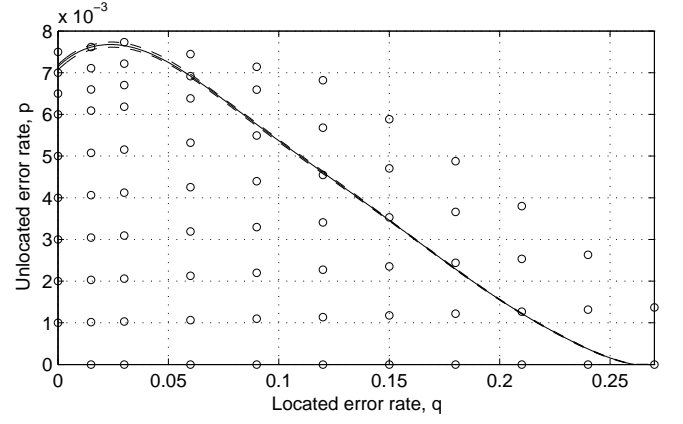


FIG. 3: Threshold region (below the solid line) for the deterministic protocol using the 23-qubit Golay code. Memory noise is disabled top, and enabled bottom. Dashed lines in upper figure show error due to finite sample size.

show an unexpected feature: the threshold for unlocated noise actually *improves* when a small amount of located noise is added. Presumably, the presence of located noise converts some crashes from unlocated to located, which are then more efficiently dealt with by higher levels of concatenation. So, although it would seem a somewhat absurd notion that adding noise should ever improve the reliability of an error-correction protocol, such behaviour in this case highlights how advantageous it can be to pass information (i.e., crash locations) from one level to another in a concatenated protocol. Such behaviour appears somewhat similar to the well-known phenomenon of stochastic resonance, whereby adding noise to a system may in some circumstances actually improve the signal-to-noise ratio in observations made on that system.

E. Final Results

In this subsection we give the final threshold results for optical cluster-state quantum computing, with respect to the physical error rates of our noise model.

Under k layers of concatenation, our error-correction protocol consists of one level of the optical cluster protocol concatenated with $k - 1$ levels of the deterministic protocol. Define the maps $f : (\epsilon, \gamma) \rightarrow (E(\epsilon, \gamma), \Gamma(\epsilon, \gamma))$ and $g : (p, q) \rightarrow (P(p, q), Q(p, q))$, where E and Γ are the polynomials obtained for the optical cluster protocol in Subsection VC7 and P and Q are the polynomials obtained for the deterministic protocol in Subsection VD5. If ϵ is the depolarization parameter and γ is the photon loss rate (defined in Section III) then the unlocated and located crash rates at level k may be estimated by computing $(g^{(k-1)} \circ f)(\epsilon, \gamma)$. If this tends to $(0, 0)$ as $k \rightarrow \infty$ then the physical noise rates (ϵ, γ) are below the threshold.

Note that in deriving the results in this section, we are imagining that the same code (either 7-qubit or 23-qubit) is used at every level of concatenation. This need not be the case, and in general it is possible to imagine a situation where the code choice is made independently at each level.

The threshold regions using the 7-qubit and 23-qubit codes are shown in Figures 4 and 5 respectively. In the upper plot in Figure 5 we have estimated the error in the threshold due to the finite sample size of the simulations, using a method similar to that of Subsection VD5. The estimated error is not shown in the other three plots, but is smaller in these cases.

The best of the four thresholds is given by the 23-qubit code with no memory noise. In this case, the protocol can simultaneously protect against a depolarization strength of 4×10^{-4} and photon loss rate of 10^{-2} , approximately. As expected, these values are poorer than for the concatenated circuit-based protocol, due to the overhead associated with clusterization of the optical protocol. We consider these values encouraging, especially given the nondeterministic nature of the optical two-qubit interactions.

F. Resource usage

In this subsection we perform a simple analysis of resource usage. This analysis is performed for the Steane 7-qubit code, and for a particular physical noise rate. Ideally, a fuller analysis would consider the (rather complex) question of how resource usage varies with physical noise rates, code choice, and other variable aspects of the protocol such as number of parallel fusions. However, the present analysis is merely aimed at giving a very rough idea of resource requirements.

For a measure of resource usage, we count the average number of Bell pairs consumed per encoded operation. This measure can also be considered as a rough indica-

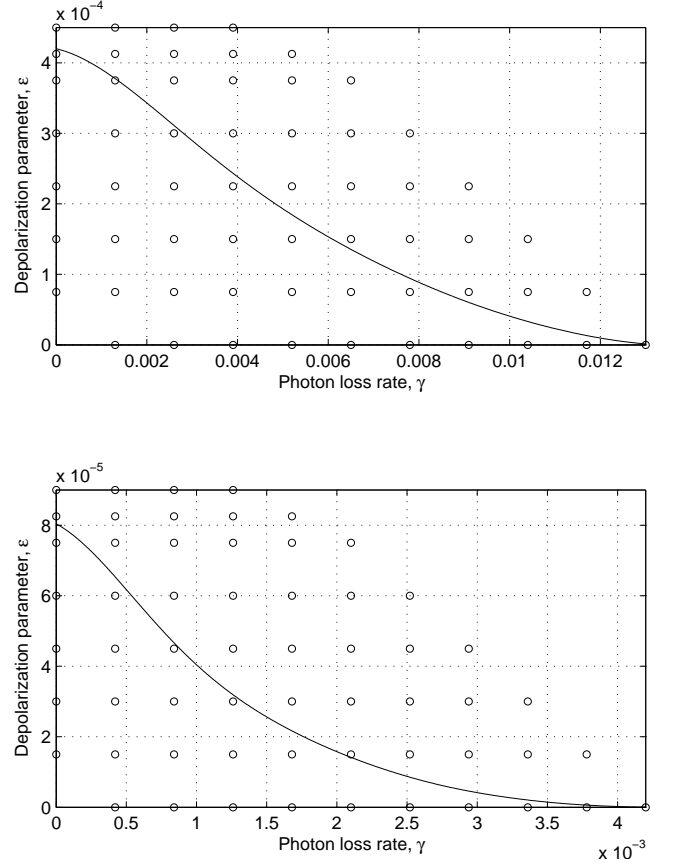


FIG. 4: Threshold region (below the solid line) for the optical cluster protocol using the 7-qubit Steane code. Memory noise is disabled top, and enabled bottom. Circles are located at the noise parameter values for which the cluster simulation was run.

tion of the usage of the other basic operations (fusion gate, measurement, memory), since in the protocol these operations are always very closely associated with Bell pair creation and vice versa.

By “per encoded operation” in the description of the resource usage measure above, we are referring to an operation at the highest level of concatenation (that is, an actual logical gate of the computation being carried out). Henceforth, we refer to such operations as “computational operations”. The resource usage figure will thus depend on the number of levels of concatenation. In turn, the number of levels of concatenation required will depend on the desired level of reliability of the final output of the computation, and the total number of computational operations performed. For the sake of the present analysis, let us define a “reliable” computation to be as follows: with probability at least $\frac{1}{2}$ all computational operations are crash-free (with respect to the highest level of encoding). Assuming noise rates are below the threshold, adding more levels of concatenation will give a lower probability of crash per computational

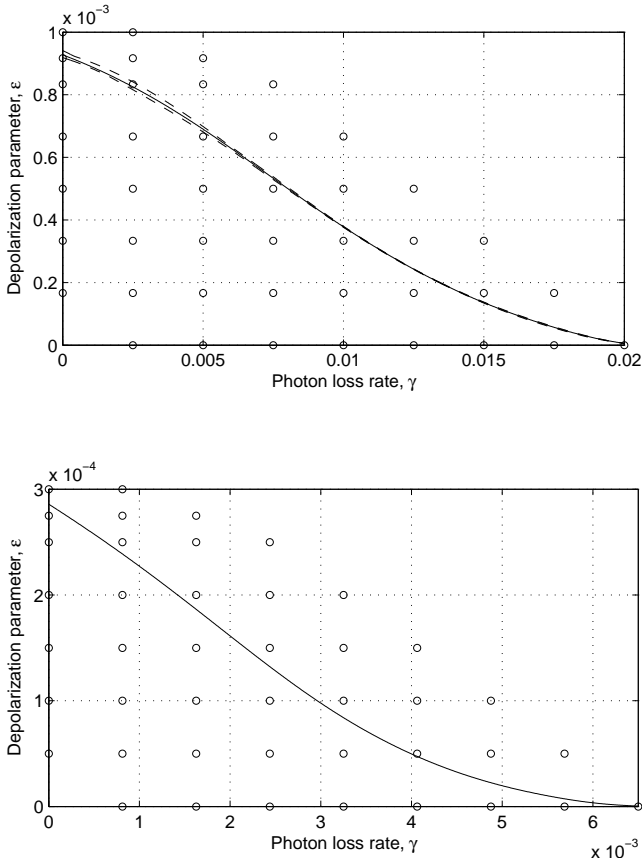


FIG. 5: Threshold region (below the solid line) for the optical cluster protocol using the 23-qubit Golay code. Memory noise is disabled top, and enabled bottom. Dashed lines in the upper figure show error due to finite sample size.

operation, and thus increase the maximum number of computational operations allowed such that the output will be reliable. If the total crash probability per computational operation is p_c , then the output will be reliable if the number of computational operations is less than

$$\frac{\log(\frac{1}{2})}{\log(1 - p_c)}. \quad (60)$$

In Table II, the results of the analysis are shown, for the 7-qubit code with memory noise enabled. The chosen physical noise parameters are $(\epsilon, \gamma) = (4 \times 10^{-5}, 4 \times 10^{-4})$, corresponding to a point roughly in the centre of the threshold region. Each row of the table corresponds to a different number of levels of concatenation. The effective rates of unknown and known crashes at each level are shown in the columns p and q . These values were obtained by iterating the polynomials generated from the numerical simulations⁸. The maximum computation

Level	p	q	Max. reliable comp. length	Bell pairs used per comp. op.
1	0.00046	0.0097	68	1.5×10^{11}
2	0.00022	0.0027	2.4×10^2	9.3×10^{13}
3	4.4×10^{-5}	0.00036	1.7×10^3	5×10^{16}
4	1.5×10^{-6}	9.9×10^{-6}	6.1×10^4	2.6×10^{19}
5	1.6×10^{-9}	9.4×10^{-9}	6.3×10^7	1.4×10^{22}
6	1.9×10^{-15}	9.8×10^{-15}	5.9×10^{13}	7.1×10^{24}

TABLE II: Estimated resource usage (number of Bell pairs consumed per computational operation) as a function of concatenation level, for noise parameters $(\epsilon, \gamma) = (4 \times 10^{-5}, 4 \times 10^{-4})$, and using the 7-qubit code.

length for each level was calculated from Equation (60) with $p_c = p + q$. The value for Bell pairs consumed per computational operation, at a particular level L , is given by the number of Bell pairs consumed per error-correction step at level 1, multiplied by appropriate scale-up factors for each of the levels $2, \dots, L$. The scale-up factor at some level l is the expected number of level $l-1$ error-correction steps used to implement a level l error-correction. These factors were estimated by the simulator in a straightforward way (the details of the estimation procedure are not given).

Thus, we see that to get a reliable computation consisting of a significant amount of operations (say 10^9), the protocol as it stands has the very demanding requirement of approximately 10^{23} Bell pairs per operation. That this figure is so large can be partly explained by our liberal use of post-selection in the various parts of the protocol. Since our main aim in this paper is to find the threshold for optical quantum computing, our protocol was designed with optimization of the threshold the primary goal, and thus optimization of resource usage was a lesser priority. A number of simple modifications to the protocol would reduce the resource usage by a few orders of magnitude at least, while only having a small detrimental effect on the threshold. Such modifications would include increasing the number of attempts per parallel fusion so that clusters are discarded less often, and spreading cluster-building procedures over more time steps so that smaller clusters are discarded if a step fails. Nonetheless, resource usage is certainly a significant problem both for our protocol and others (especially those that heavily rely on post-selection such as [44] and [23]).

⁸ For the purposes of this analysis, we disallowed further low-order

terms in the polynomial that by the principles of fault tolerance should be zero. This was done with the aim of increasing the accuracy for very small parameter values.

VI. CONCLUSION

In this paper we’ve done a detailed numerical investigation of the fault-tolerant threshold for optical cluster-state quantum computing. Our work considers a noise model which allows for both photon loss and depolarizing noise. Depolarizing noise is used as a general proxy for all types of local noise other than photon loss, and standard results in the theory of error-correction ensure that the ability to protect against depolarization ensure the ability to protect against other types of noise, including dephasing, amplitude damping, etc.

Our main result has been a *threshold region* of allowed pairs of values for the photon loss and depolarizing noise. Roughly speaking, our results show that scalable optical quantum computing is possible for photon loss probabilities $< 3 \times 10^{-3}$, and for depolarization probabilities $< 10^{-4}$. To achieve such threshold values requires very substantial overheads in order to accurately perform long computations. Future work will need to not only improve the threshold, but also reduce the overhead required to do fault-tolerant computation, improve the accuracy of the noise model used in simulations, and address the pseudethreshold phenomenon identified in [45, 46].

Our noise model is in contrast to previous investigations of the threshold for optical quantum computing, which have focused on the case in which photon loss is the *sole* source of noise. While photon loss will certainly be an important source of noise in real implementations, other sources of noise such as dephasing will also be present (at lower levels), and techniques which protect solely against photon loss will have the effect of greatly amplifying those other sources of noise. Thus, while the earlier loss-only thresholds are of considerable theoretical interest, they do not provide physically meaningful thresholds.

We note that our threshold results might be applicable to implementations of quantum computing other than linear optics – in particular to any scheme that contains nondeterministic two-qubit interactions, loss noise and depolarization noise. For example, in the scheme by Barret and Kok [47] for quantum computing with matter qubits, two-qubit interactions are nondeterministic, with a heralded failure rate of 50%. In analogy to photon loss, the scheme can also exhibit “loss” when an atom jumps out of the qubit space into a higher energy level. It is likely that our threshold results would agree at least qualitatively with the thresholds for such a system.

Acknowledgments

Many thanks to Maries Hankel of the CCMS computing facility. Thanks to Ike Chuang, Jennifer Dodd, Steve Flammia, and Tim Ralph for helpful discussions. Thanks to Peiter Kok for helpful correspondence. We thank Bryan Eastin and Steve Flammia for their circuit drawing package *Qcircuit*.

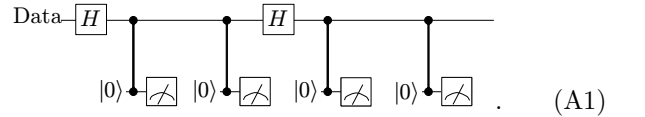
APPENDIX A: TELECORRECTION

This appendix presents the idea of the telecorrector in a simple form, without the baggage of clusters and non-determinism. Although use of the telecorrector arises naturally from the cluster state model, there are good reasons to consider it in the circuit model as well. First, it provides a different way of thinking about quantum error correction: most of the difficulty of a fault tolerant round of quantum error correction can be reduced to the creation of a single $2n$ -qubit resource state (n being the size of the code). This is in contrast to the normal requirements of an error correction round – the creation of a variable number (at least four) copies of an n -qubit ancilla state. While we shall consider a particular way of generating the telecorrector, based on a teleported Steane syndrome extraction circuit, it is an interesting open problem to consider better methods for creation.

The second reason for considering telecorrection in the circuit model is for practical use in our simulations. Our deterministic error correction protocol, used for the second and higher levels of concatenation, uses circuit-model telecorrection instead of the standard Steane approach. The benefit is an improved threshold, due to the ability to post-select for agreeing syndromes and against located noise types during telecorrector creation.

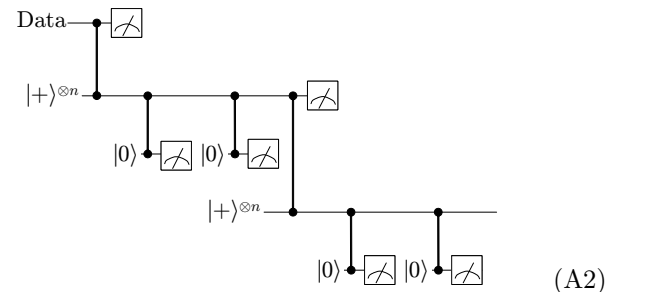
Note that the idea of combining error correction and teleportation has been used previously by Knill [23], however the details of our telecorrection procedure and Knill’s procedure differ significantly in the details.

We now derive a circuit for fault-tolerant telecorrection. Begin with the following circuit for Steane’s repeated syndrome extraction:

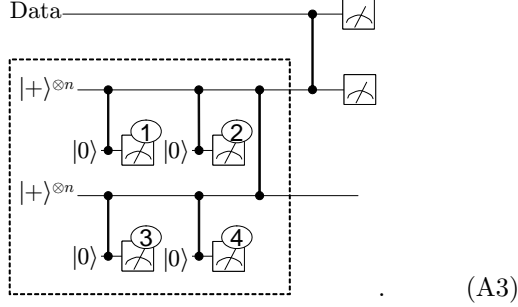


In the circuit, wires and gates represent encoded qubits and encoded operations respectively, and $|0\rangle$ represents Steane’s fault-tolerant ancilla creation circuit. The circuit performs two Z syndrome extractions followed by two X syndromes, and generalizes to more than two extractions of each in the obvious way.

We replace each of the encoded Hadamard operations in Circuit (A1) by the transport circuit of Equation (3), to give



where we have omitted showing the necessary classical feed-forward associated with the transport steps. We commute various operations to finally give



The dashed box encloses the telecorrector creation circuit. Measurements 1 and 2 correspond to Z syndrome measurements of the original circuit, and measurements 3 and 4 correspond to X syndrome measurements. However, these measurements do not directly give the syndromes of the input data, since they must be adjusted due to the output of the transport-circuit measurements. The details of this will be derived below. Note however that we can determine if the syndromes of like type will agree, and post-select for this, before the telecorrector has interacted with the data.

To understand exactly what state the telecorrector is, we now consider the evolution of Circuit (A3), in the case of noise-free operations. The telecorrector creation circuit begins with the state $|+\rangle^{\otimes n} \otimes |+\rangle^{\otimes n}$. We note that the state $|+\rangle^{\otimes n}$ can be written, without normalization, as

$$|+\rangle^{\otimes n} = \sum_{s=0}^{2^{(n-1)/2}-1} \vec{X}(s) |+\rangle_L, \quad (\text{A4})$$

where s labels X -syndromes of the code (we are assuming the code encodes one qubit, hence there are $2^{(n-1)/2}$ X -syndromes), $\vec{X}(s)$ is some tensor product of X s and I s having syndrome s , and $|+\rangle_L$ is the encoded $|+\rangle$ state. Each $|+\rangle^{\otimes n}$ in the circuit undergoes two X syndrome extractions, each consisting of a controlled phase with an encoded $|0\rangle$ ancilla and subsequent measurement. The first X syndrome extraction performed on a $|+\rangle^{\otimes n}$ randomly collapses it to one of the terms in Equation (A4). In the noise-free case, the second syndrome extraction has no effect. Thus, the state of the telecorrector after all syndrome extractions, but before the controlled phase connecting the two halves, is

$$\left(\vec{X}(s_z) |+\rangle_L \right) \otimes \left(\vec{X}(s_x) |+\rangle_L \right), \quad (\text{A5})$$

where s_z and s_x represent the syndrome measurement results from the top and bottom halves of the circuit respectively.

Next we apply the controlled phase between the two halves of the telecorrector creation circuit. This gives the state

$$\left(\vec{X}(s_z) \vec{Z}(s_x) \otimes \vec{X}(s_x) \vec{Z}(s_z) \right) | \bigcirc - \bigcirc \rangle, \quad (\text{A6})$$

where we have commuted the controlled phase through the X operations, and the ket is the encoded two-node cluster state. Thus, a noise-free telecorrector state is an encoded two-node cluster state, up to known Pauli operations.

We now consider the remaining operations in Circuit (A3) that complete the telecorrection of the data. The controlled phase between the telecorrector and data gives the state

$$\left(\vec{Z}(s_z) \otimes \vec{X}(s_z) \vec{Z}(s_x) \otimes \vec{X}(s_x) \vec{Z}(s_z) \right) | \psi - \bigcirc - \bigcirc \rangle, \quad (\text{A7})$$

where the ket is the state (on encoded qubits) obtained by applying a controlled phase between the data state, denoted ψ , and a two-node cluster state.

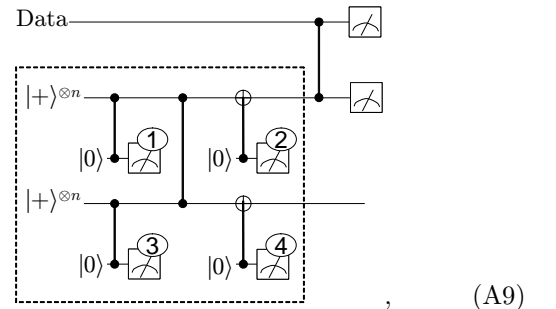
The final two measurements are then performed. These are encoded X -basis measurements on the data and one half of the telecorrector. An encoded X -basis measurement is performed by measuring each physical qubit in the X basis, adjusting the measurement results to remove the effects of known Pauli operations ($\vec{Z}(s_z)$ in the case of the measurement of the data, and $\vec{Z}(s_x)$ in the case of the measurement of the top half of the telecorrector), and performing classical error correction on the resulting bit string. For the codes we consider, the measurement outcome is 0 if the corrected bit string has even weight, and 1 otherwise. The corrections performed during the two encoded measurements have the effect of eliminating any errors present in the input state, and also certain errors introduced by telecorrector creation, subject to the weight of those errors being not too large.

Let the measurement result on the data and telecorrector be m_1 and m_2 respectively. Then, the output state is

$$\vec{X}(s_x) \vec{Z}(s_z) (Z^{\otimes n})^{m_1} (X^{\otimes n})^{m_2} |\psi\rangle, \quad (\text{A8})$$

to which we apply the appropriate Pauli operators, giving the final output of the telecorrector, the error-corrected version of the state $|\psi\rangle$.

Finally, note that the following straightforward modification to the telecorrection circuit,



provides an improved noise-threshold performance compared with Circuit (A3). In Circuit (A9), measurements 1 and 4 correspond to Z syndrome extraction in Steane's

protocol, and measurements 2 and 3 correspond to X syndrome extraction. The circuit has the property that the post-selection for preagreeing syndromes will eliminate a larger class of errors than is the case for Circuit (A3). For example, X errors which propagate from either ancilla 1 and 3 to become Z errors on the telecor-

rector will very likely cause syndromes 2 or 4 to disagree with 3 or 1 respectively. Also, certain types of noise caused by a failed controlled phase between the two halves of the telecorrector will also cause disagreeing syndromes.

-
- [1] Y. Yamamoto, M. Kitagawa, and K. Igeta, in *Proc. 3rd Asia-Pacific Phys. Conf.* (World Scientific, Singapore, 1988).
 - [2] G. J. Milburn, Phys. Rev. Lett. **62**, 2124 (1989).
 - [3] E. Knill, R. Laflamme, and G. J. Milburn, Nature **409**, 46 (2001).
 - [4] T. B. Pittman, M. J. Fitch, B. C. Jacobs, and J. D. Franson, Phys. Rev. A **68**, 032316 (2003).
 - [5] J. L. O'Brien, G. J. Pryde, A. G. White, T. C. Ralph, and D. Branning, Nature **426**, 264 (2003).
 - [6] K. Sanaka, T. Jennewein, J.-W. Pan, K. Resch, and A. Zeilinger, Phys. Rev. Lett. **92**, 017902 (2004).
 - [7] S. Gasparoni, J.-W. Pan, P. Walther, T. Rudolph, and A. Zeilinger, Phys. Rev. Lett. **93**, 020504 (2004), arXiv:quant-ph/0404107.
 - [8] Z. Zhao, A.-N. Zhang, Y.-A. Chen, H. Zhang, J.-F. Du, T. Yang, and J.-W. Pan, Phys. Rev. Lett. **94**, 030501 (2005), arXiv:quant-ph/0404129.
 - [9] J. D. Franson, M. M. Donegan, M. J. Fitch, B. C. Jacobs, and T. B. Pittman, Phys. Rev. Lett. **89**, 137901 (2002), arXiv:quant-ph/0202160.
 - [10] A. Gilchrist, A. J. F. Hayes, and T. C. Ralph, arXiv:quant-ph/0505125 (2005).
 - [11] M. A. Nielsen, Phys. Rev. Lett. **93**, 040503 (2004).
 - [12] N. Yoran and B. Reznik, Phys. Rev. Lett. **91**, 037903 (2003).
 - [13] R. Raussendorf and H. J. Briegel, Phys. Rev. Lett. **86**, 5188 (2001).
 - [14] D. E. Browne and T. Rudolph, Phys. Rev. Lett. **95**, 010501 (2005).
 - [15] P. Walther, K. J. Resch, T. Rudolph, E. Schenck, H. Weinfurter, V. Vedral, M. Aspelmeyer, and A. Zeilinger, Nature **434**, 169 (2005).
 - [16] P. Kok, W. J. Munro, K. Nemoto, T. C. Ralph, J. P. Dowling, and G. J. Milburn, arXiv:quant-ph/0512071 (2005).
 - [17] M. A. Nielsen and I. L. Chuang, *Quantum computation and quantum information* (Cambridge University Press, Cambridge, 2000).
 - [18] M. A. Nielsen and C. M. Dawson, Phys. Rev. A **71**, 052312 (2005).
 - [19] R. Raussendorf, Ph.D. thesis, Ludwig-Maximilians Universität München (2003), <http://edoc.ub.uni-muenchen.de/archive/00001367>.
 - [20] P. Aliferis and D. W. Leung, arXiv:quant-ph/0503130 (2005).
 - [21] R. Raussendorf, J. Harrington, and K. Goyal, arXiv:quant-ph/0510135 (2005).
 - [22] C. M. Dawson, H. L. Haselgrove, and M. A. Nielsen, Phys. Rev. Lett. **96**, 020501 (2006), arXiv:quant-ph/0509060.
 - [23] E. Knill, Nature **434**, 39 (2005).
 - [24] A. M. Steane, Phys. Rev. A **68**, 042322 (2003).
 - [25] M. Varnava, D. E. Browne, and T. Rudolph, arXiv:quant-ph/0507036 (2005).
 - [26] T. C. Ralph, A. J. F. Hayes, and A. Gilchrist, Phys. Rev. Lett. **95**, 100501 (2005), arXiv:quant-ph/0501184.
 - [27] R. Raussendorf, D. E. Browne, and H. J. Briegel, Phys. Rev. A **68**, 022312 (2003).
 - [28] M. A. Nielsen, arXiv:quant-ph/0504097 (2005), to appear in Rev. Math. Phys.
 - [29] X. Zhou, D. W. Leung, and I. L. Chuang, Phys. Rev. A **62**, 052316 (2000), arXiv:quant-ph/0002039.
 - [30] E. Knill, R. Laflamme, and W. H. Zurek, Proc. Roy. Soc. A **454**, 365 (1998), arXiv:quant-ph/9702058.
 - [31] P. W. Shor, in *Proceedings, 35th Annual Symposium on Fundamentals of Computer Science* (IEEE Press, Los Alamitos, 1996), pp. 56–65.
 - [32] D. Aharonov and M. Ben-Or, in *Proceedings of the Twenty-Ninth Annual ACM Symposium on the Theory of Computing* (1997), pp. 176–188.
 - [33] D. Aharonov and M. Ben-Or, arXiv:quant-ph/9906129 (1999).
 - [34] P. Aliferis, D. Gottesman, and J. Preskill, arXiv:quant-ph/0504218 (2005).
 - [35] D. Gottesman, Phys. Rev. A **57**, 127 (1998), arXiv:quant-ph/9702029.
 - [36] D. Gottesman, Ph.D. thesis, California Institute of Technology, Pasadena, CA (1997), arXiv:quant-ph/9705052.
 - [37] J. Preskill, Proc. Roy. Soc. A: Math., Phys. and Eng. **454**, 385 (1998).
 - [38] B. W. Reichardt, arXiv:quant-ph/0509203 (2005).
 - [39] A. Y. Kitaev, in *Quantum Communication, Computing, and Measurement*, edited by A. S. H. O. Hirota and C. M. Caves (Plenum Press, New York, 1997), pp. 181–188.
 - [40] B. M. Terhal and G. Burkard, Phys. Rev. A **71**, 012336 (2004), arXiv:quant-ph/0402104.
 - [41] A. Steane, arXiv:quant-ph/0202036 (2002).
 - [42] S. Ling and C. Xing, *Coding Theory – A First Course* (Cambridge University Press, 2004).
 - [43] D. Terr, *Golay code*, from *Mathworld*, URL <http://mathworld.wolfram.com/GolayCode.html>.
 - [44] B. W. Reichardt, arXiv:quant-ph/0406025 (2004).
 - [45] K. M. Svore, B. M. Terhal, and D. P. DiVincenzo, Phys. Rev. A **72**, 022317 (2005), arXiv:quant-ph/0410047.
 - [46] K. M. Svore, A. W. Cross, I. L. Chuang, and A. V. Aho, arXiv:quant-ph/0508176 (2005).
 - [47] S. D. Barrett and P. Kok, Phys. Rev. A **71**, 060310 (2005), arXiv:quant-ph/0408040.